Up, down, and round again: the circulating flow dynamics of flux-driven fractures

C.M. Chalk[1] and J.L. Kavanagh[1]

1.Department of Earth, Ocean and Ecological Sciences, University of Liverpool, Liverpool L69 3GP, United Kingdom

(*Electronic mail: cmchalk@liverpool.ac.uk)

Fluid-filled fracture propagation is a complex problem that is ubiquitous in Geosciences, from controlling magma propagation beneath volcanoes to water transport in glaciers. Using scaled analogue experiments, we characterized the internal flow inside a propagating flux-driven fracture and determined the relationship between flow and fracture evolution. Different flow conditions were created by varying the viscosity and flux (Q) of a Newtonian fluid injected into an elastic solid. Using particle image velocimetry we measured the fluid velocity inside the propagating fracture and mapped the flow across the crack plane. We characterized the internal flow behavior with the Reynolds number (Re) and explored Re values spanning five orders of magnitude, representing very different internal force balances. The overall fracture tip propagation velocity is a simple linear function of Q, whereas the internal velocity, and Re, may be vastly different for a given Q. We identified four flow regimes – viscous, inertial, transitional, and turbulent – and produced viscous and inertial regimes experimentally. Both flow regimes exhibit a characteristic flow pattern of a high-velocity central jet that develops into two circulating vortices on either side. However, they exhibit the opposite behavior in response to changing Q: the jet length increases with Q in the inertial regime, yet decreases in the viscous regime. Spatially variable, circulating flow is vastly different from the common assumption of unidirectional fracture flow, and has strong implications for the mixing efficiency and heat transfer processes in volcanic and glacial applications.

I. INTRODUCTION

Fluid-filled fracture propagation is a fundamental process in many geoscience applications, including magma transport[1–3], glacier dynamics and stability[4–6], and geothermal energy systems[7–9]. Magma-filled fractures (dykes and fissures) feed volcanic eruptions, whilst glacial fractures (crevasses) control the drainage of glacial lakes and the transport of melt water. The fluid dynamics within propagating fractures has a significant effect on the overall fracture behavior. Propagation is driven by internal fluid pressure (due to fluid injection, buoyancy, or a combination of the two), which is distributed and dissipated by the internal flow[10]. In dykes and fissures, the flow of magma influences the style of eruption at the surface[11,12]. Flow in glacial crevasses can have a significant impact on glacier stability and melting rates[13–15]. Understanding and predicting fracture behaviour, including the expected pathway, propagation rate, and internal fluid dynamics, is essential for managing the risks associated with volcanic and climate change processes. Despite its importance, the fluid flow within propagating fractures is not well understood, and is typically assumed to be unidirectional — a key assumption of many theoretical and numerical models of fracture propagation[2,16–18].

A major challenge in modelling fracture propagation and internal fluid flow is having a unified understanding of the full range of potential behaviour. Some theoretical and numerical models models neglect fluid flow and assume that buoyancy dominates, and have been able to recreate fracture pathways in experiments and in nature[19,20]. However, buoyancy-driven fractures only represent a subset of natural cases, and fluid flow must be included to obtain accurate predictions of propagation velocities[16,17]. Flux-driven fractures are driven by the pressure created by fluid injection, where buoyancy may not play any role[2,21,22]. In theoretical and numerical models of flux-driven fractures, flow, as characterised by the dimensionless Reynolds number Re, is typically assumed to be in one of two limiting regimes: viscosity-dominated[2,23–25] ($Re \ll 1$) or turbulent[26–28] ($Re > 1000$). In reality, fracture flow spans a wide range of regimes due to the vast natural parameter space, notably the fluid viscosity. Fluid in glacial fractures and geothermal systems has a viscosity of the order 10^{-3} Pa s, yet for magma this varies between 10^{-2} Pa s (for ultramafic low-silica magmas) and 10^{9} Pa s (for evolved, silica-rich rhyolite)[29]. In nature, Reynolds numbers range from the order of 10^{-10} for viscous, creeping dykes[30], to 10^{6} and beyond for turbulent crevasses during rapid drainage events[5]. There is therefore a strong motivation to understand fracture propagation for the full range of potential flow regimes and Re values, particularly in the transition from viscosity-dominated flows to full turbulence[28,31].

Scaled, analogue experiments of fluid-filled fracture propagation give crucial insight into the fundamental processes of fracture dynamics (see Rivalta et al. (2015)[17] and Kavanagh et al. (2018)[32] for a review). Laboratory experiments involving the injection of fluid into solid, elastic, gelatine allow for direct observations of fracture and fluid dynamics during propagation[33,34]. Buoyancy-driven fracturing occurs if the injected fluid is sufficiently less dense than the solid host[35–38]. Otherwise, flux-driven fractures are created by the constant injection of fluid[22,32,39]. Recent studies have used Particle Image Velocity (PIV) to measure internal flow velocity profiles in flux-driven fractures[32,40,41]. Whilst flow in buoyancy-dominated fractures is confirmed to have a simple unidirectional profile[41], Newtonian flux-driven fractures exhibit a more complex flow pattern, consisting of a central, localized jet, with circulating downflow along the fracture margins[32,40,41], which is not captured with any existing numerical model. Only a small number of published experiments (all consisting of water injections with Reynolds numbers in the narrow range $1 \leq Re \leq 30$) have captured this interesting flow pattern. Experimental data across a wider Re range is required to fully understand flux-driven fracture propagation and the influence of internal fluid flow.

In this study, we provide the first experimental investigation of the dependence of fracture dynamics on the Reynolds number. We restrict our attention to flux-driven fractures (that are not buoyant) and conduct a series of experiments where a Newtonian fluid is injected into gelatine at a constant rate. We systematically vary Re by changing the viscosity of the injected fluid and its injection rate, achieving flows in the range $O(10^{-3}) \leq Re \leq O(10^{2})$. Propagation velocities and internal fluid flow profiles are measured across a two-dimensional plane of the growing fracture for the full duration of the experiment. Our results showcase the complex fluid dynamics inside flux-driven fractures and the relationship with propagation velocities. A jet and recirculation is a universal feature of Newtonian flux-driven flows, yet there are key differences between viscous and inertial flow regimes. We discuss the physics behind this observed behavior and the implications for natural flux-driven fractures in glacial and magmatic settings.

II. THEORETICAL FRAMEWORK

In this section we present the relevant theoretical framework behind the experimental flux-driven fractures, particularly related to the internal fluid flow (the main focus of this study). We consider the following simplifications: a single, vertical fracture is driven by a constant continuous flux; the host is an isotropic, non-porous, elastic solid; the injected fluid is Newtonian and non-buoyant; fractures are tensile, opening in the direction of the least compressive stress σ_3. We adopt Linear Elastic Fracture Mechanics (LEFM)[3,42], and assume that the solid resistance to fracture is characterized by the fracture toughness K_C (Pa/m$^{1/2}$). Fracture propagation occurs if the stress intensity K at the tip (a function of fluid pressure gradients) equals a critical value K_C. We assume that K_C is constant, although experiments suggest that K_C may change with fracture length[37]. These simplifications are common assumptions in mathematical and numerical models of flux-driven fractures[2,18,43,44].

A. Equations of fluid motion

Flux-driven fracture propagation requires the continuous injection of fluid as this provides a driving pressure gradient at the source, which is distributed to the fracture tips via fluid flow. The evolution of pressure and fluid flow are governed by the Navier-Stokes equations, consisting of the conservation of mass and momentum:

$$\nabla \cdot \boldsymbol{u} = 0, \tag{1}$$

$$\rho_f \frac{\partial \boldsymbol{u}}{\partial t} + \rho_f \boldsymbol{u} \cdot \nabla \boldsymbol{u} = -\nabla p + \mu \nabla^2 \boldsymbol{u}. \tag{2}$$

Here $\boldsymbol{u} = (u_x, u_z)$ is the fluid velocity, ρ_f is the fluid density, p is the dynamic fluid pressure (i.e. excess of hydrostatic), t is time, and μ is dynamic viscosity. Along with suitable boundary conditions, Equations (1) and (2) describe incompressible, Newtonian flow inside a flux-driven fracture.

1. Boundary conditions

Injection of fluid can be expressed as a flux boundary condition:

$$\boldsymbol{u} \cdot \boldsymbol{n} = \frac{Q}{A}, \; \textit{at the inlet}, \tag{3}$$

where $\boldsymbol{n}$ is the unit normal direction to the inlet flow, Q is the volumetric flux (m^3/s) and A (m^2) is the area of the inlet surface ($\mathscr{I}$). $\frac{Q}{A}$ is the fluid injection velocity, also written as u_{in}. Note that Equation 3 is equivalent to imposing a pressure gradient at the inlet.

Fluid flow satisfies the no-slip condition:

$$\boldsymbol{u} = \boldsymbol{u}_{tip}, \; at\ the\ solid-fluid\ interface, \tag{4}$$

where $\boldsymbol{u}_{tip}$ is the velocity of the fracture tip.

2. Fluid forces

In the momentum equation (2), dynamic pressure gradients (units of force per unit volume, N/m^3) are balanced with two forces, viscous ($\boldsymbol{F}_V = (F_{Vx}, F_{Vz})$) and inertial ($\boldsymbol{F}_I = (F_{Ix}, F_{Iz})$):

$$\nabla p = \boldsymbol{F}_I - \boldsymbol{F}_V \tag{5}$$

$$\boldsymbol{F}_I = \rho_f \frac{\partial \boldsymbol{u}}{\partial t} + \rho_f \boldsymbol{u} \cdot \nabla \boldsymbol{u}, \tag{6}$$

$$\boldsymbol{F}_V = \mu \nabla^2 \boldsymbol{u}. \tag{7}$$

In addition to driving fracture growth, the imposed pressure gradient due to fluid injection is also dissipated by viscous and inertial forces.

B. Opposing pressure scales

The forces that oppose fracture propagation can be represented by simple pressure scales[2,37,41,43,44]. Solid resistance to fracture is represented by the fracture pressure scale P_f:

$$P_f \sim \frac{K_C}{\min(L,W)^{1/2}}, \tag{8}$$

where $\min(L,W)$ is the minimum of the fracture length L and width W.

The viscous pressure scale ΔP_V represents the drop in pressure along the fracture due to viscous resistance:

$$\Delta P_V \sim \frac{3\mu u L}{H^2}, \tag{9}$$

where μ is viscosity, H is the fracture thickness and u is the average internal velocity. This scaling (9) follows from the Navier-Stokes equations (1) (2) under lubrication theory assumptions: laminar, unidirectional flow with negligible inertia[1,2,18,25].

In high Re flows inertial effects are important and pressure is dissipated via fluid kinetic energy[45]. The inertial pressure scale ΔP_I is derived through neglecting viscosity from the full equations of fluid motion. ΔP_I represents the loss of fluid pressure to inertial forces:

$$\Delta P_I \sim \frac{f_D \rho_f u^2 L}{2}, \tag{10}$$

where f_D is a complex empirical function of the friction factor and fracture geometry[5,46]. Closures for (10) have been proposed for turbulent fracture flow[5,26], yet there is very little focus on the transition from viscosity-dominated laminar flow and full turbulence[46].

C. Dimensionless numbers

Flux-driven fractures propagate in different regimes according to the dominant resistive processes. Fractures in gelatine are expected to propagate in the toughness regime[32,37], where the dominant opposing pressure scale is the fracture pressure P_F. In the toughness regime, the solid fracture process uses more energy than fluid forces, yet the relative balance of internal inertial and viscous forces still influences the overall fracture dynamics[17,47]. Denoting the characteristic flow velocity with $\mathscr{U}$ and the characteristic length scale with $\mathscr{L}$, the magnitude of the fluid force terms can be estimated as[48]:

$$|\boldsymbol{F}_I| = |\rho_f \boldsymbol{u} \cdot \nabla \boldsymbol{u}| \sim \frac{\rho_f \mathscr{U}^2}{\mathscr{L}} \tag{11}$$

$$|\boldsymbol{F}_V| = |\mu \nabla^2 \boldsymbol{u}| \sim \frac{\mu \mathscr{U}}{\mathscr{L}^2}, \tag{12}$$

The Reynolds number Re represents the ratio of inertial to viscous forces:

$$Re = \frac{|\rho_f \boldsymbol{u} \cdot \nabla \boldsymbol{u}|}{|\mu \nabla^2 \boldsymbol{u}|} = \frac{\rho_f \mathscr{U} \mathscr{L}}{\mu}. \tag{13}$$

For fracture flows, $\mathscr{L}$ is the fracture thickness H, and $\mathscr{U}$ can be approximated as $\mathscr{U} \approx Q/WH$[41,49]. This reduces Re to:

$$Re_0 = \frac{\rho_f Q}{\mu W}. \tag{14}$$

In the toughness regime, two dimensionless numbers describe the relative effects of viscous and inertial forces to the fracture resistance. These are known as the dimensionless viscosity μ_k and dimensionless inertia R_k:

$$\mu_k = \frac{12 \mu Q'}{E'} \left(\frac{E'}{K'} \right)^4 \tag{15}$$

$$R_k = \frac{\rho_f E'^{5/3} Q'^{5/3}}{K'^{8/3} t^{1/3}}, \tag{16}$$

where $Q‘ = Q/W$ is the volumetric flux per unit width (m^2/s) and

$$E‘ = \frac{E}{1-\nu^2}, \; K‘ = 4\sqrt{2/\pi} K_C, \tag{17}$$

where E is the Young's modulus and ν is Poisson's ratio. Note that R_k is a decreasing function of time, whilst μ_k is constant. R_k and μ_k were derived from an idealized, plane-strain, flux-driven fracture model that quantifies the coupled effects of fracture resistance, viscosity and inertia[27]. We expect μ_k and R_k to be small (< 1) in the toughness regime as fracture resistance dominates.

III. METHODOLOGY

Here we describe the experimental process in detail. We first provide an overview of the experimental set-up and the materials used, followed by a description of the PIV method for measuring internal fracture velocities during propagation. We then provide details on post-processing the experimental data, including the calculation of representative fracture velocities, forces, and Reynolds numbers.

A. Overview

A series of experiments were conducted to establish the effect of Re on both the internal fluid dynamics and the overall propagation of flux-driven fractures. Each experiment consists of a Newtonian fluid being injected into a $40 \times 40 \times 25$ cm^3 volume of transparent, solid, elastic gelatine held in a clear Perspex tank. An initial, vertical, pre-cut of 3 cm length and 1 cm width is created in the centre of the base of the gelatine using a thin blade. The fluid is injected into the pre-cut using a needle with its tapered edge orientated parallel to the widest part of the pre-cut. The needle has an inlet diameter d of either 1 or 2 mm and an elliptical opening surface area A of either $\pi \times 1 \times 3.5$ mm^2 or $\pi \times 2 \times 4$ mm^2. The needle is connected to a fluid reservoir via 5 mm diameter tubing. A valve on the pipe and a small amount of petroleum jelly added to the end of the needle ensures all air is removed from the injection system prior to starting an experiment. A peristaltic pump then pushes fluid through the tube and into the gelatine at a known, constant rate, creating a flux-driven penny-shaped fracture that propagates vertically and erupts at the surface through a thin fissure. The pre-cut controls the fracture orientation, ensuring it grows vertically in the z direction and radially in the $x-z$ plane, whilst pushing open the solid as a tensile fracture in the $y-z$ plane (see Fig.1). Two-dimensional (2D) internal velocity profiles are measured in the $x-z$ plane using a laser-based particle image velocimetry (PIV) system (see Sec. III C), controlled via LaVision's DaVis 10 specialized laser imaging software[50,51]. The laser-imaging system and experimental tank are all supported by a robust, connected metal frame that ensures experiment repeatability.

B. Materials

Different flow regimes were achieved by injecting Newtonian fluids with different viscosity but similar density: a high viscosity fluid (silicone oil, $\mu = 0.45$ Pa s, $\rho_f = 998$ kg/m^3), and a low viscosity fluid (water, $\mu = 0.001$ Pa s, $\rho_f = 998$ kg/m^3). The viscosity of silicone oil was determined with a series of rheometer tests at different temperatures, and the density was obtained using a 100 ml pycnometer.

The solid, elastic gelatine had a concentration of 2.5 wt % and was prepared following the guidelines of Kavanagh et al.[32,52], resulting in 1001.5 kg/m^3 solid density[32]. Gelatine preparation involves mixing 1 kg of gelatine powder (260 Bloom, 10 mesh, pig-skin gelatine supplied by Gelita UK) with 39 kg of deionised water, resulting in a total liquid mass of 40 kg. Approximately half of the total amount of water was added hot (≈ 80 °C) to initially dissolve the gelatine, and the rest was added cold ($\approx 7-10$ °C) directly in the tank. The liquid mixture was then covered in a thin layer of vegetable oil and covered with plastic wrapping. It was left to cool and solidify in a refrigerator for approximately 41-50 hours to obtain a Young's modulus E in the range 3000-5000 Pa (note that the addition of cold water allowed for shorter solidification times than if using hot water only). E was measured immediately before running an experiment using the method of Kavanagh et al.[52], which involves removing the surface oil and then applying different loads to the centre of the gel surface and measuring their deflections. Gelatine's fracture toughness K_C can be approximated as $K_C = 1.4\sqrt{E}$[52].

C. The PIV system

Planar PIV is used to measure horizontal and vertical fluid velocities inside the fracture in the $x-z$ plane. The injected fluid is pre-seeded with Rhodamine B-coated tracer particles with diameters of $d_p = 20-50$ μm and a particle density of $d_p = 1190$ kg/m^3. Calculations of Stokes settling velocity U_g, relaxation time τ_r, and Stokes number St suggest that these particles suitably trace the fluid streamlines (see Sec. I in the Supplementary Material). Successive images of these passive tracer particles are used to track fluid motion and compute velocities (see the videos in the

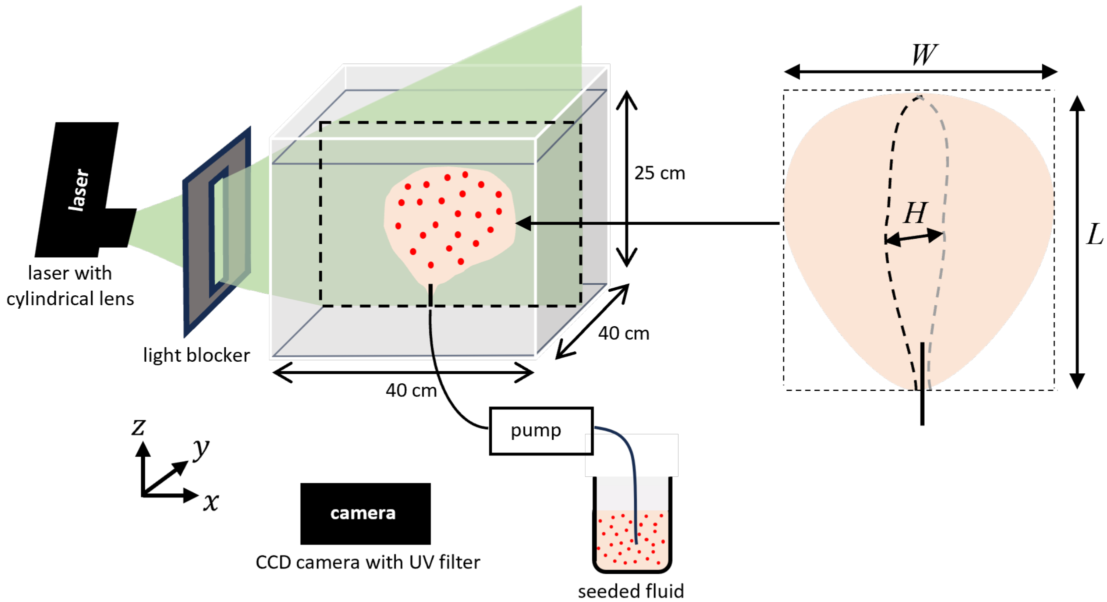

FIG. 1. Schematic of the experimental set-up depicting a growing flux-driven penny-shaped fracture being illuminated with a laser sheet.

Supplementary Material). The PIV method[53] divides each image into subdomains of a defined size (here either 32×32 or 24×24 pixels), and applies a statistical correlation technique to produce a single velocity vector per subdomain (with a calculation overlap of 75% between subdomains). The time interval between recorded images is chosen so that there is optimal particle displacement between successive images (of approximately 5 pixels[51]). PIV has been used to measure velocities in laboratory flows with a wide variety of geophysical applications[32,54–58].

The tracer particles are fluoresced with a sheet of light emitted from a Class 4 532nm DoublePulse Nd:YAG Litron laser (maximum energy 2x325 mJ), which illuminates the expected plane of fracture growth. Laser output is synchronized to an Imager SX 6M CCD camera facing the $x-z$ plane, positioned perpendicular to the light sheet. The camera has a resolution of 2752×2200 pixels and is used with a Zeiss 50mm f/1.4 lens with an aperture of f/5.6. The lens is fitted with a UV filter that blocks out short wavelengths and prevents reflections from the gelatine. Note that when measuring 2D flow, the light sheet should be as thin as possible to reduce out-of-plane motion effects. However, the fracture needs to remain within the sheet to ensure that the tracer particles are recorded (it is not guaranteed to be perfectly vertical). We used a 5mm-thick light sheet as a compromise between reducing potential three-dimensional (3D) effects and ensuring flow visualization. The laser is output through a -25mm convex cylindrical lens (from Edmund Optics Ltd).

Magnetic blockers (with an adjustable gap in the middle) positioned between the laser output and tank wall transform the laser light into a thin sheet, orientated along the centre of the tank (see Fig.1).

Images are captured in either single-frame or double-frame mode[53], depending on the expected magnitude of particle displacements (Tab. I). In single-frame mode, each image consists of a single frame that records the emission of two laser pulses with an exposure time of 42 μs. The shortest time interval that can be achieved between subsequent frames in single-frame mode is restricted by the maximum camera frame rate of 15 frames per second. However, double-frame recordings allow for shorter time intervals. In double-frame mode, each image is composed of two frames separated by an interval Δt, which is achieved via control of the camera shutter. This also defines the separation between the two laser pulses, so that the first frame captures the first emission, and the second frame captures the second pulse. The exposure of the first frame is defined by Δt, whereas the exposure of the second frame cannot be controlled and may capture more ambient light. For this reason, double-frame recordings are performed with the overhead room lights turned off. The recording settings for each experiment are provided in Tab. I in the Supplementary Material.

Prior to running an experiment, the camera is first focused on fluoresced particles in a tank full of seeded water, with the laser and camera in position. A calibration procedure is then performed (within the Davis software) where images are taken of a calibration board positioned in the imaging plane. Pixels are automatically converted to material coordinates in subsequent DaVis operations. The calibration procedure is conducted prior to running an experiment, and requires that the camera and laser positions are kept at a fixed position relative to the tank and imaging plane – this is ensured via the supportive frame.

D. Data processing

1. Post-processing PIV data

Erroneous PIV velocity vectors were removed in 'Vector Post-Processing' in DaVis[50] according to a threshold set by the correlation value r_c (the degree of confidence in the statistical correlation procedure). A threshold of $r_c = 0.2$ eliminated vectors lying outside of the seeded fracture flow.

Velocity data were exported from DaVis as a series of csv files (one for each time step), containing the velocity components u_x, u_z and the corresponding spatial coordinates x, z. All further analysis was performed in Matlab[59]. Data were imported using the `readtable` function, and each variable was converted to a 2D grid and processed with median filtering and Gaussian smoothing functions (`medfilt2` and `smoothdata`). Velocity data collected in single-frame mode were time averaged over an interval representing 5% of the experimental duration, resulting in an averaged velocity profile and standard deviation. Double-frame velocity data were not time averaged due to the time separation between two successive images being greater than 5%. All processing scripts are available in an accompanying data publication[60].

2. Tracking fracture geometry

The fracture outline was extracted from the raw images by cropping around the illuminated particles. Images were first converted to binary using `im2bw` (from the `Image Processing Toolbox`[61]), and an appropriate pixel intensity threshold is selected to distinguish black from white. The binary image was reduced in size and outliers removed, before applying the `rangesearch` function (in the `Statistics and Machine Learning Toolbox`[62]) to remove individual pixels with fewer than a specified number of neighbours. The `boundary` function is applied to detect the bounding shape of the reduced set of pixels, which is then converted to material coordinates. An ellipse was fitted to the boundary points (with function `fitellipse`[63]). Fracture length L and width W were calculated from the length and width of the fitted ellipse at its centre point.

3. Representative velocities

Different representative velocities are used to characterize the fracture at a given time, including tip velocities and internal flow velocities. Tip velocities consist of the fracture propagation rate in the vertical and horizontal directions – u_{tip} and u_W respectively. Representative flow velocities include the spatially-averaged mean velocity u_{mean}, a representative jet velocity u_{jet}, a representative downwards velocity u_{down}, and a circulation velocity[41] u_{circ}. The latter represents the degree of internal flow circulation: $u_{circ} = (u_{jet} - u_{down})/u_{jet}$. A value of $u_{circ} = 1$ means that there is zero downwards flow and no circulation, whilst $u_{circ} = 2$ corresponds to the downwards velocity being of equal magnitude to the upwards velocity, indicating strong circulation.

To obtain values for u_{jet}, vectors within the jet region were systematically cropped in each experiment and averaged in this area (within the 65-90 percentile range); a comparison with full velocity contours confirms that this method gives a velocity value that is representative of the jet. A similar method was applied to get u_{down}, where the data were instead cropped near the lateral fracture margins, and filtered according to $u_z < 0$. Tip velocities $u_{tip} = dL/dt$ and $u_W = dW/dt$ were calculated by first fitting third-order polynomials to the temporal evolution of L and W, before integration over t. Error terms for u_{jet}, u_{mean} and u_{down} were calculated using the corresponding velocity standard deviation terms (note that these errors could be obtained for the non-time-averaged double-frame experiments W2-W4). Errors for u_{tip} and u_W were approximated by considering the difference between the temporal geometry data (L,W) and their fitted curves.

4. Calculating fluid forces and pressure scales

For each experiment, the viscous and inertial forces (7) can be calculated using the measured velocity data $\boldsymbol{u}_{i,j}$. Here, $\boldsymbol{u}_{i,j}$ denotes a single PIV grid measurement where indices i and j represent the spatial location in the x and z directions respectively. Adjacent grid points are separated by a constant distance Δx in both directions. Two adjacent points are denoted by $\boldsymbol{u}_{i,j}$ and $\boldsymbol{u}_{i+1,j}$ in the x axis, and $\boldsymbol{u}_{i,j}$ and $\boldsymbol{u}_{i,j+1}$ in the z axis. First and second order velocity derivatives are calculated using a finite difference method[64], and substituted into (7) to obtain approximations of inertial and viscous forces at a given time. These forces have a horizontal and vertical component (in 2D), such that $\boldsymbol{F}_v = (F_{Vx}, F_{Vz})$ and $\boldsymbol{F}_I = (F_{Ix}, F_{Iz})$. The numerical (finite difference) approximations of the force terms (denoted with a ˆ notation) are defined as:

$$\hat{F}_{Vxi,j} \approx \frac{\mu}{\Delta x^2}\left(u_{xi-1,j} + u_{xi+1,j} + u_{xi,j-1} + u_{xi,j+1} - 4u_{xi,j}\right), \tag{18}$$

$$\hat{F}_{Vzi,j} \approx \frac{\mu}{\Delta x^2}\left(u_{zi-1,j} + u_{zi+1,j} + u_{zi,j-1} + u_{zi,j+1} - 4u_{zi,j}\right), \tag{19}$$

$$\hat{F}_{Ixi,j} \approx \rho_f \frac{\partial u_{xi,j}}{\partial t} + \frac{\rho_f}{\Delta x}\left(u_{xi,j}\left(u_{xi+1,j} - u_{xi,j}\right) + u_{zi,j}\left(u_{xi,j+1} - u_{xi,j}\right)\right), \tag{20}$$

$$\hat{F}_{Izi,j} \approx \rho_f \frac{\partial u_{zi,j}}{\partial t} + \frac{\rho_f}{\Delta x}\left(u_{xi,j}\left(u_{zi+1,j} - u_{zi,j}\right) + u_{zi,j}\left(u_{zi,j+1} - u_{zi,j}\right)\right). \tag{21}$$

These terms are spatially-averaged across the full fracture profile to approximate the average (absolute) forces (viscous $\bar{\boldsymbol{F}}_V$ and inertial $\bar{\boldsymbol{F}}_I$) at a given time:

$$|\bar{\boldsymbol{F}}_V| = \frac{1}{N-1}\sum_{i=2}^{N-1}|\hat{\boldsymbol{F}}_{Vi,j}| \tag{22}$$

$$|\bar{\boldsymbol{F}}_I| = \frac{1}{N-1}\sum_{i=2}^{N-1}|\hat{\boldsymbol{F}}_{Ii,j}|, \tag{23}$$

where N is the total number of grid points and $|\hat{\boldsymbol{F}}_{Vi,j}|$ and $|\hat{\boldsymbol{F}}_{Ii,j}|$ denote the modulus of the numerical viscous and inertial force terms at a single point.

Estimates of the viscous and inertial pressure scales are then obtained by multiplying the average force by the fracture length:

$$\Delta\hat{P}_V \approx |\bar{\boldsymbol{F}}_V|L \tag{24}$$

$$\Delta\hat{P}_I \approx |\bar{\boldsymbol{F}}_I|L. \tag{25}$$

E. Reynolds number calculations

The Reynolds number summarizes the bulk flow behavior as a single parameter, yet in reality flow can be spatially and temporally variable, with a range of characteristic velocity and length scales. In addition to $Re_0 = \frac{\rho_f Q}{\mu W}$ (14), we explore several alternative Reynolds numbers using different characteristic velocities and length scales, that may potentially better represent the force balance during fracture flow. We define four alternative Reynolds numbers: 1) the inlet Reynolds number, Re_{in}, 2) the tip Reynolds number, Re_{tip}, 3) the jet Reynolds number, and 4) Re_{jet}, and the mean Reynolds number Re_{mean}. The flow at the source of fluid injection is characterized by Re_{in}, and is known prior to running an experiment. Flow Reynolds numbers Re_{tip}, Re_{jet} and Re_{mean} represent the internal flow during fracture propagation, and require measured velocity values (see Sec. III D 3).

1. Inlet Reynolds number, Re_{in}

Re_{in} represents the fluid force balance at the inlet, and does not require any information about the fracture flow or geometry. This is defined as:

$$Re_{in} = \frac{\rho_f u_{in} d}{\mu}. \tag{26}$$

2. Tip Reynolds number, Re_{tip}

Re_{tip} uses the vertical fracture tip velocity u_{tip} as the characteristic velocity scale, and H as the length scale:

$$Re_{tip} = \frac{\rho_f u_{tip} b}{\mu}. \tag{27}$$

3. Jet Reynolds number, Re_{jet}

Re_{jet} represents the internal flow behavior, with the characteristic velocity defined as the jet velocity u_{jet}:

$$Re_{jet} = \frac{\rho_f u_{jet} b}{\mu}. \tag{28}$$

4. Mean Reynolds number, Re_{mean}

Re_{mean} also represents the internal flow, but instead uses the mean internal velocity u_{mean} as the characteristic value:

$$Re_{mean} = \frac{\rho_f u_{mean} b}{\mu}. \tag{29}$$

5. Fracture thickness measurements H

The fracture thickness H is required to calculate the representative flow Reynolds numbers, Re_0, Re_{mean}, Re_{jet}, Re_{tip}. We conducted experiments to approximate H for low-viscosity, water fractures and high-viscosity silicone oil fractures respectively. The fracture evolution was instead recorded in the $y-z$ plane, either using a seeded fluid or a seeded gelatine (with no fluid seeding, see Sec. III in the Supplementary Material). The representative thickness was approximated via manual image inspection within the DaVis software.

IV. RESULTS

In total, eleven experiments were completed with Re_{in} ranging from 0.009 to 633 (Tab. I). All experiments produced a broadly penny-shaped fluid-filled crack that grew and eventually erupted at the surface. Nine experiments measured fluid velocities in the $x-z$ plane (five silicon oil (S) and four water (W) injections) and two experiments measured a representative H for the different fluid injections (one for silicone oil (SH), and one for water (WH)) (see Tab. II). All silicone oil injections have $Re_{in} < 1$, whilst the water injections all have $Re_{in} > 1$. The fracture thickness H varies with height, and measurements of H may be affected by optical distortions related to out-of-plane fracture growth and mismatching refractive indices between the fluid and gelatine (see Sec. II in the Supplementary Material). We therefore report a conservative range of H values: $H \approx 3-5$ mm for water, and $H \approx 7-15$ mm for silicone oil (S experiments have a high refractive index mismatch and a larger error margin, as a closer refractive index matching leads to more accurate measurements). These variations in H have a minor effect on the overall change in Reynolds number, and the average H value was used in Re calculations.

In the following sections we present the fluid flow profiles, temporal fracture evolution, and governing force balance results. Note that in these descriptions our main focus is the developed flow pattern (the initial flow development is presented in Fig. 3 in the Supplementary Material). To allow for a direct comparison between different experiments, time is normalized as $t^* = (t - t_0)/t_{erupt}$, where t_0 is the time when $L = 10$ cm and t_{erupt} is the time interval between t_0 ($t^* = 0$) and fluid eruption ($t^* = 1$).

A. Flow profiles — central jet and recirculation

Every experiment produced a high-velocity central jet that increased in width with height, before transitioning to a recirculating flow on either side of the jet, around two stagnant points (Fig. 2, $t^* = 0.5$). There is a strong spatial velocity variation, with u_{jet} being the most dominant characteristic flow velocity and ranging from 0.379 to 236 mm/s across all experiments (Tab. II, $t^* = 0.5$). u_{jet} is at least one order of magnitude greater than the tip velocities in every experiment (which range from 0.021 to 3.676 mm/s at $t^* = 0.5$).

Whilst all experiments have the same overall pattern of a jet and recirculating flow, there are some clear differences between the $Re_{in} < 1$ and $Re_{in} > 1$ experiments (Figs. 2 and 3). In the $Re_{in} < 1$ experiments (S1-S5), flow is mostly localized in the central jet region, and the downward flow velocities are significantly lower than in the jet. In these experiments, the jet terminates prior to reaching the vertical fracture tip, and an increase in Re_{in} correlates with a decrease in the jet height. Conversely, in all $Re_{in} > 1$ experiments (W1-W4) the jet reaches the vertical fracture tip and recirculates along the upper boundary, distributing high velocities throughout the fracture profile. An increase in Re_{in} leads to a stronger degree of downwards flow and recirculation.

TABLE I. Solid and fluid material parameters for experiments S1-5 and SH (injecting silicone oil), experiments W1-W4 and WH (injecting water). Young's modulus E (Pa), gelatine concentration c_g (wt%), volumetric flux Q (m^3/s), fluid viscosity (μ), fluid density ρ_f (kg/m^3), inlet diameter d (mm), thickness H (mm) (including range and associated experiment), inlet Reynolds number Re_{in}.

	E	Q	μ	ρ_f	d	H	Re_{in}
S1	4337	4.37×10^{-8}	0.450	998	1	11.5 (7-15, SH)	0.009
S2	4098	7.20×10^{-8}	0.450	998	1	11.5 (7-15, SH)	0.015
S3	4170	1.34×10^{-7}	0.450	998	1	11.5 (7-15, SH)	0.027
S4	4506	2.60×10^{-7}	0.450	998	2	11.5 (7-15, SH)	0.046
S5	4214	4.07×10^{-7}	0.450	998	1	11.5 (7-15, SH)	0.092
W1	4309	4.68×10^{-7}	0.001	998	1	4 (3-5, WH)	36.650
W2	2593	3.15×10^{-6}	0.001	998	2	4 (3-5, WH)	250.088
W3	3591	6.97×10^{-6}	0.001	998	1	4 (3-5, WH)	633.005
W4	2278	6.97×10^{-6}	0.001	998	1	4 (3-5, WH)	633.005
SH	3946	4.07×10^{-7}	0.450	998	1	11.5 (7-15)	0.092
WH	3591	6.97×10^{-6}	0.001	998	1	4 (3-5)	633.005

Along the central jet region, all experiments show an increase in velocity with height up to the normalized location of the velocity maximum, $\hat{z}_{max}$. Above $\hat{z}_{max}$, the velocity decreases with height as it approaches u_{tip} (Fig. 3A, $t^* = 0.5$). All $Re_{in} < 1$ experiments have a particularly steep velocity increase up to $\hat{z}_{max}$, which decreases from approximately 0.4 to 0.1 for experiments S1 to S5 respectively, thus indicating the decrease in the jet height with increasing Re_{in} for $Re_{in} < 1$. As the $Re_{in} > 1$ experiments have a longer jet than the $Re_{in} < 1$ experiments, their velocity maximum is higher at $\hat{z}_{max} \approx 0.5$ and the profiles are more or less symmetric about $\hat{z}_{max}$. (for all $Re_{in} > 1$ experiments).

The normalized horizontal velocity line profiles highlight the focused flow around the jet region — which has the same relative thickness for all experiments — and the local velocity minima on either side. They collapse onto one another in the central jet region at $t^* = 0.5$ (Fig. 3B). The secondary velocity peaks represent the downwards circulating flow, which is significantly stronger for $Re_{in} > 1$. Whilst the central jet velocity dominates the flow in all experiments, W3 and W4

TABLE II. Flux-driven fracture thickness and characteristic velocity results for each experiment, at a dimensionless time of $t^* = 0.5$: inlet velocity u_{in} (mm/s), thickness H (mm) (including range and associated experiment), vertical tip velocity u_{tip} (mm/s), horizontal tip velocity u_W (mm/s), mean velocity u_{mean} (mm/s), jet velocity u_{jet} (mm/s), downflow velocity u_{down} (mm/s), $\frac{\partial u_{mean}}{\partial t}$ (mm/s^2), $\frac{\partial u_{jet}}{\partial t}$ (mm/s^2).

	u_{in}	u_{tip}	u_W	u_{mean}	u_{jet}	u_{down}	$\frac{\partial u_{mean}}{\partial t}$	$\frac{\partial u_{jet}}{\partial t}$
S1	3.975	0.023	0.021	0.050	0.379	-0.053	6.6×10^{-7}	4.4×10^{-5}
S2	6.551	0.040	0.023	0.084	0.686	-0.088	5.7×10^{-7}	5.3×10^{-5}
S3	12.209	0.076	0.054	0.124	1.229	-0.119	5.8×10^{-6}	3.3×10^{-4}
S4	10.347	0.258	0.308	0.247	1.925	-0.183	3.3×10^{-4}	0.0032
S5	41.430	0.147	0.182	0.233	1.591	-0.106	1.1×10^{-4}	6.6×10^{-4}
W1	36.724	0.236	0.171	2.432	6.907	-2.573	5.5×10^{-4}	-0.0042
W2	125.295	1.418	1.480	30.601	135.641	-58.565	0.052	-0.19
W3	634.273	2.539	2.929	108.404	211.867	-153.974	-0.60	1.36
W4	634.273	3.676	3.517	82.717	235.844	-124.827	-1.49	-0.80

reach particularly high downwards velocities of around 60% of the maximum value.

B. Characteristic velocities

Characteristic flow velocities ($u_{jet}, u_{down}, u_{mean}$) are nonlinear functions of Q, exhibiting a unique relationship for the two sets of experiments $Re_{in} < 1$ and $Re_{in} > 1$. In both cases, internal velocities initially increase with Q, before appearing to reach a limiting value. This is in contrast to the vertical tip velocity u_{tip}, which is a linear function of Q (Fig. 4, $t^* = 0.5$). The approximate inlet velocity u_{in} does not increase linearly with Q for all experiments due to differences in the size of the injection needle. However, when comparing u_{in} and u_{tip}, it's clear that u_{tip} is less than 1% of u_{in} at any given time (see Tab. II, and Fig. 2 in the Supplementary Material). Although u_{tip} is a linear function of Q overall, $S4$ has greater tip velocities than $S5$ at all times (Fig. 5A,B), despite having a lower Q. S4 contained a trapped air bubble at the fracture tip, which we interpret to have enhanced its overall propagation rate.

When $Re_{in} < 1$, u_{mean} and $|u_{down}|$ have similar values to u_{tip}, which all lie in the range 0.02 – 0.25 mm/s (Fig. 4 and Tab. II). The simple velocity approximation Q/WH is also very similar

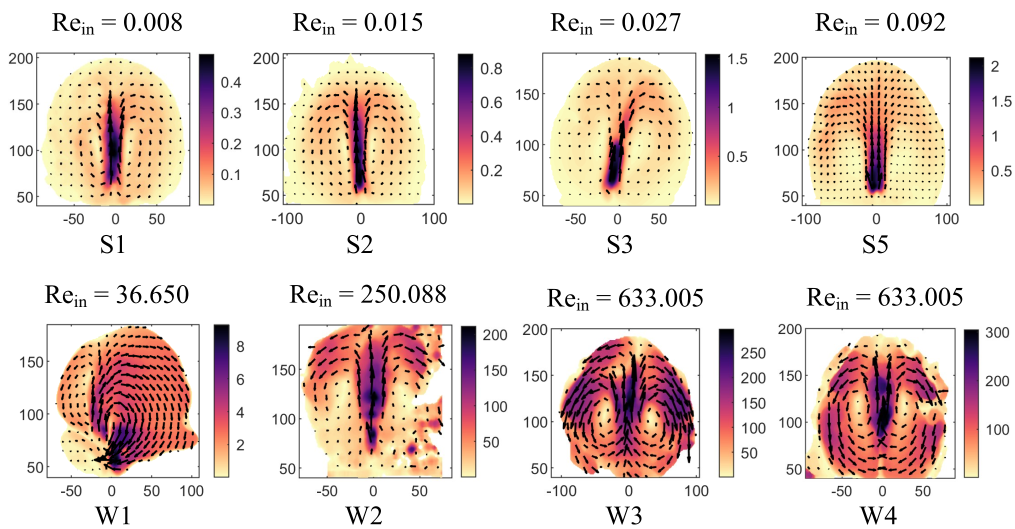

FIG. 2. Filled contours of velocity magnitude (mm/s) and vectors of flow direction (black arrows) for flux-driven fracture experiments, at a normalized time of $t^* = 0.5$. Four of the high-viscosity $Re_{in} < 1$ silicone oil experiments (S1-S3,S5) are shown on the top row, and the low-viscosity $Re_{in} > 1$ experiments (W1-W4) are on the bottom row. For each row, the experiments are ordered in terms of increasing Q and Re_{in}. The vectors show the flow direction, and their size represents the velocity magnitude, scaled up by a factor of two. Only every third vector is plotted (horizontally and vertically), whilst the filled contours show the full resolution of the flow velocity magnitude.

to u_{tip}, u_{mean} and u_{down}. When $Re_{in} > 1$, u_{mean} and u_{down} are significantly closer in value to u_{jet} than u_{tip}. The simple velocity approximation Q/WH is larger than u_{tip} when $Re_{in} > 1$, but still significantly under-predicts the mean internal flow.

C. Temporal evolution of characteristic velocities

Overall, all experiments exhibit a similar pattern in terms of the temporal behavior of different characteristic velocities (Fig. 5). The nine experiments have a widely dispersed range of fracture tip velocities in the vertical (u_{tip}) and horizontal (u_W) directions (Fig. 5A and 5B), however, when normalized they show consistent behavior. In all cases, u_{tip} initially decreases, then reaches a short-lived state of steady propagation around $t^* = 0.5$ (Fig. 5C) and finally increases to eruption. In contrast, u_W decreases rapidly until near-eruption when it approaches a steady value (Fig. 5D). In the initial stage of propagation, $u_{tip}/u_W < 1$ for all experiments except S4 (Fig. 5E). The two velocities then approach one another (at a different t^* value for each experiment), after which u_{tip}

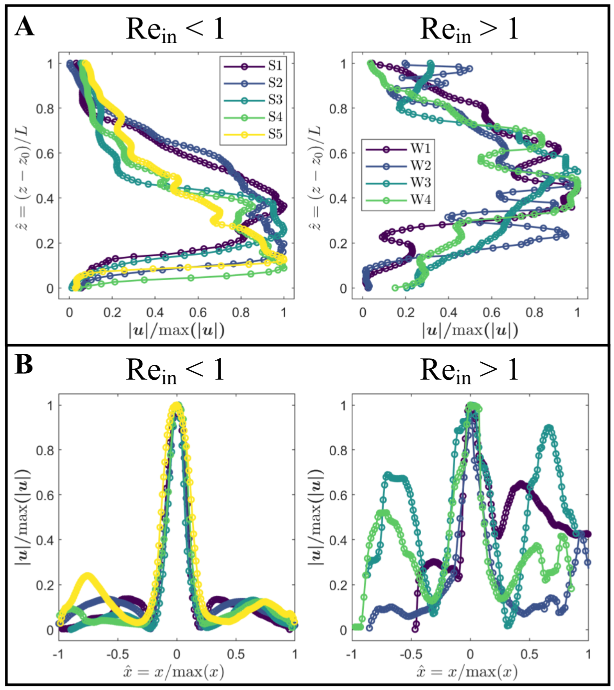

FIG. 3. Normalized velocity magnitude profiles at $t^* = 0.5$: (A) along the central vertical line above the injector and (B) along a horizontal line 60 mm above the injector, for silicon oil (S1-S5, $Re_{in} < 1$) and water (W1-W4, $Re_{in} > 1$) experiments. Height has been normalized so that $\hat{z} = 0$ is just above the injector, and $\hat{z} = 1$ is the tip location. In the vertical profiles, the pentagon denotes the fracture tip velocity. The horizontal distance has been normalized so that the $\hat{x} = 0$ corresponds to the location of the maximum velocity and the horizontal extent is between $\hat{x} = \pm 1$.

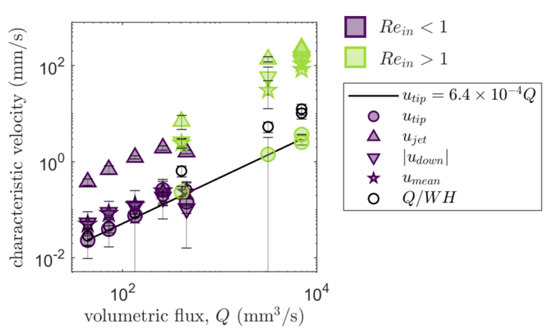

FIG. 4. Characteristic fracture velocities (tip velocity u_{tip}, jet velocity u_{jet}, absolute downwards velocity $|u_{down}|$, mean velocity u_{mean}, mm/s) relative to the volumetric flux Q (mm^3/s) at a dimensionless time of $t^* = 0.5$. Experiments with $Re_{in} < 1$ are shown in purple, and $Re_{in} > 1$ experiments are shown in green. The line of best fit between u_{tip} and Q is shown for all experiments ($u_{tip} = 6.4 \times 10^{-4}$ Q).

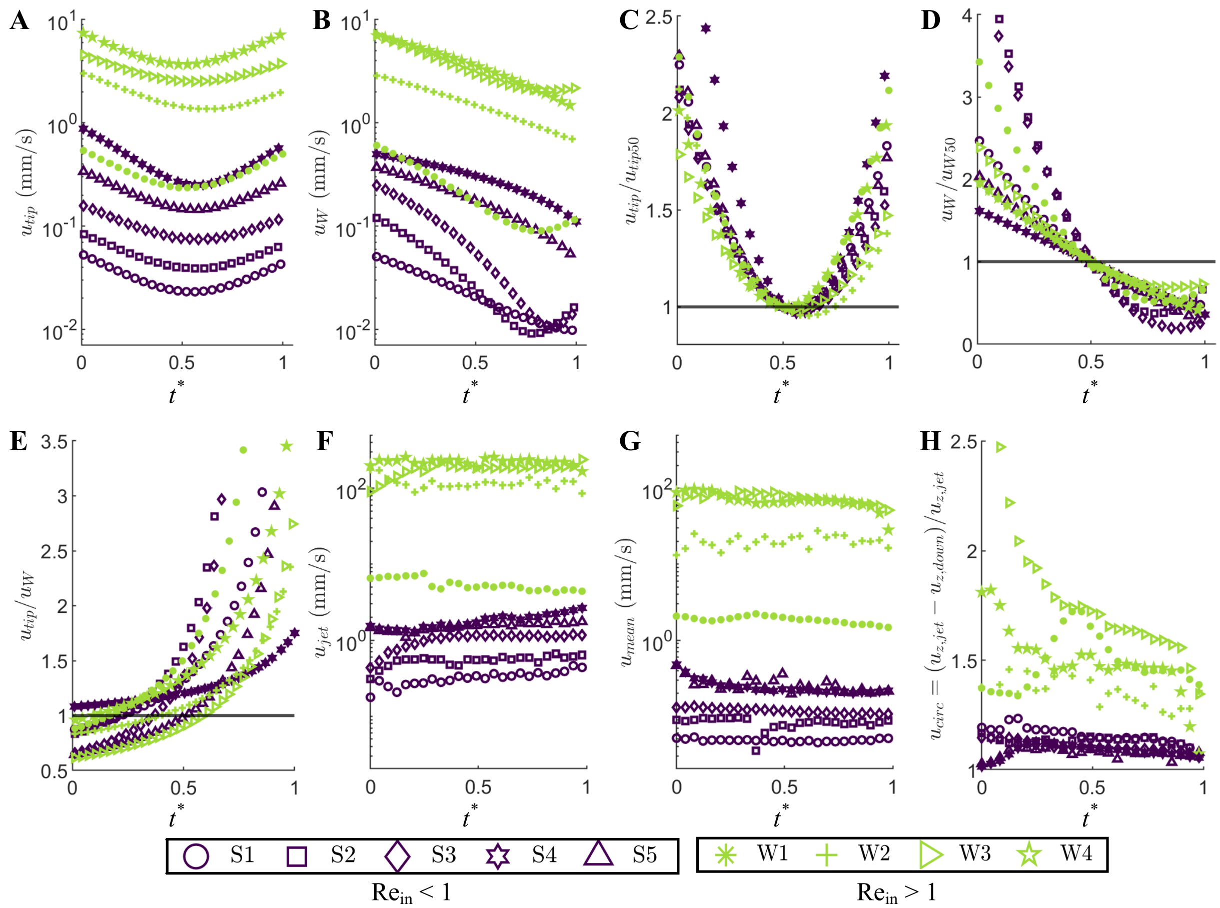

FIG. 5. Evolution of characteristic fracture velocities (purple = silicon oil, green = water) with normalized time t^*. A) Fracture tip velocity in the vertical direction , u_{tip}, B) Velocity of crack breadth increase (horizontal tip velocity, u_W) , C) Normalized u_{tip} (according to u_{tip50}, the mean velocity at $t^* = 0.5$), D) Normalized u_W (according to u_{W50}, the mean horizontal tip velocity at $t^* = 0.5$, E) Ratio of vertical to horizontal tip propagation velocities (u_{tip}/u_W), F) Internal jet flow velocities (from PIV) u_{jet}, G) Mean absolute velocities (from PIV) u_{mean}, and H) Flow circulation velocities (from PIV) $u_{circ} = (u_{jet} - u_{down})/u_{jet}$, where $u_{circ} = 2$ indicates strong circulation.

significantly exceeds u_W up until eruption.

Compared to temporal variations in tip velocities, temporal variations in internal velocities are generally insignificant (Fig. 5F,G, Tab. II). Depending on the experiment, u_{mean} and u_{jet} are either approximately constant in time (e.g. S1 and S2 where $\partial u_{jet}/\partial t$ $O(10^-7)$ and S2), or vary slowly in time (e.g. S4 where $\partial u_{jet}/\partial t \approx 0.0032$ mm^2/s). Accelerations were approximated as the gradient of the linear curve fitted to the temporal velocity data plotted in Fig. 5F,G (reported in Tab. II).

TABLE III. Characteristic Reynolds numbers for each experiment: Re_{in}, Re_0, Re_{tip}, Re_{mean}, Re_{jet}

	Re_{in}	Re_0	Re_{tip}	Re_{mean}	Re_{jet}
S1	0.009	6.05×10^{-4}	5.91×10^{-4}	0.001	0.010
S2	0.015	9.70×10^{-4}	9.93×10^{-4}	0.002	0.017
S3	0.027	0.002	0.002	0.004	0.030
S4	0.046	0.004	0.007	0.007	0.048
S5	0.092	0.006	0.004	0.006	0.039
W1	36.65	2.401	0.973	9.964	28.680
W2	250.088	19.991	6.541	131.081	549.470
W3	633.005	38.205	10.284	439.670	845.773
W4	633.005	46.563	17.713	339.39	941.492

Experiments with $Re_{in} > 1$ (W experiments) exhibit a strong initial degree of circulation ($u_{circ} \approx 2$, and $u_{circ} > 2$) that decreases in intensity over time (Fig. 5H). In the early stages of experiment W3, $u_circ > 2$ and the downwards flow is faster than the jet flow. When $Re_{in} < 1$ (S experiments), u_{circ} is small for the entire duration of the experiment (with a maximum value of 1.1 to 1.2 in the early stages that very gradually decreases over time)

D. Force balance during fracture propagation

Re_{jet} is consistently higher than the alternative Re definitions (Tab. III), as u_{jet} is the largest characteristic velocity (Tab. II). Re_{jet} is most similar to Re_{in}, despite u_{in} being significantly greater than u_{jet} (Tab. II). In all experiments, Re_{tip} is one order of magnitude smaller than Re_{jet} and Re_{in}, reflecting the small u_{tip} values compared to u_{jet} (Fig. 4). When $Re_{in} < 1$, Re_{mean} is very similar to Re_{tip}. Conversely, when $Re_{in} > 1$, Re_{mean} is the same order of magnitude as Re_{jet} and Re_{in}. When $Re_{in} < 1$, Re_{tip}, Re_{jet} and Re_{mean} reach limiting values (all < 0.05) with increasing Re_{in}. When $Re_{in} > 1$, Re_{tip}, Re_{jet} and Re_{mean} do not (yet) reach a limiting value with increasing Re_{in}.

Variations of the mean viscous and inertial forces ($|\bar{\boldsymbol{F}}_V|$ and $|\bar{\boldsymbol{F}}_I|$, see Equation (7)) with respect to Re_{in} are shown in Fig. 7. As expected, viscous forces dominate over inertial when $Re_{in} < 1$ ($|\bar{\boldsymbol{F}}_V| > |\bar{\boldsymbol{F}}_I|$), and conversely, inertial forces dominate over viscous when $Re_{in} > 1$ ($|\bar{\boldsymbol{F}}_I| > |\bar{\boldsymbol{F}}_V|$). When $Re_{in} \ll 1$, $|\bar{\boldsymbol{F}}_V|$ scales linearly with increasing Re_{in}, whilst $|\bar{\boldsymbol{F}}_I|$ scales with Re_{in}^2. At the

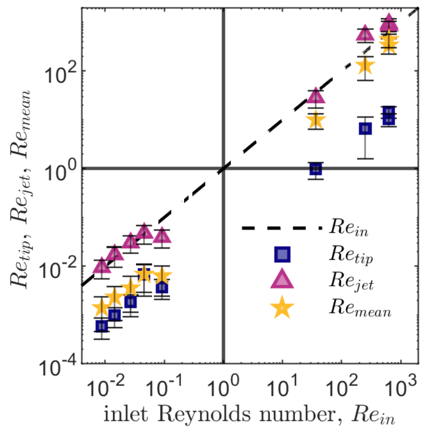

FIG. 6. The relationship between alternative flow Reynolds number (Re_{tip} (blue squares), Re_{jet} (pink triangles) and Re_{mean} (yellow stars)) and the inlet Reynolds number, Re_{in}. The dashed line depicts Re_{in}, and the solid lines show $Re = 1$. All calculations are made using velocity measurements at $t^* = 0.5$. Error bars are shown, which incorporate the error from velocity and H measurements.

highest Re_{in} value less than one (experiment S5), $|\bar{\boldsymbol{F}}_V|$ and $|\bar{\boldsymbol{F}}_I|$ deviate from this pattern. Naturally, for $Re_{in} \approx 1$, the two forces are expected to be of similar magnitude. Therefore, in the transitional region between $Re_{in} < 1$ and $Re_{in} > 1$, curves of $|\bar{\boldsymbol{F}}_V|$ and $|\bar{\boldsymbol{F}}_I|$ will cross over — $|\bar{\boldsymbol{F}}_V|$ decreases, whilst $|\bar{\boldsymbol{F}}_I|$ continues to increase. However, there are not enough data points in this region to determine how the forces behave during the transition. When $Re_{in} \gg 1$, $|\bar{\boldsymbol{F}}_V|$ and $|\bar{\boldsymbol{F}}_I|$ scale linearly with Re_{in}. At the lowest Re_{in} value greater than one (experiment W1), $|\bar{\boldsymbol{F}}_I|$ and $|\bar{\boldsymbol{F}}_V|$ deviate from the linear scaling law.

The fracture pressure P_f is the largest resistive pressure in all experiments, which decreases with time (Fig. 8, showing S3 and W4 as representative low and high Re_{in} experiments respectively). The viscous pressure drop $\Delta\hat{P}_V$ (approximated numerically, Equation (24)) has a similar magnitude for S3 and W4, despite these experiments having very different Re_{in} values. For S3 ($Re_{in} = 0.027$), the lubrication theory approximation of the viscous pressure drop (ΔP_V, Equation (9)) is similar to the numerical profile, and both increase with t^* (and L). For W4 ($Re_{in} = 633.005$), ΔP_V is considerably larger than $\Delta\hat{P}_V$, which remains approximately constant over time. The inertial pressure drop $\Delta\hat{P}_I$ (Equation (25)) is negligible for experiment S3, yet it is of the same order of magnitude as P_f in W4. Before $t^* = 0.5$, $\Delta\hat{P}_I$ increases slightly in W4 before decreasing after this (at a faster rate then P_f).

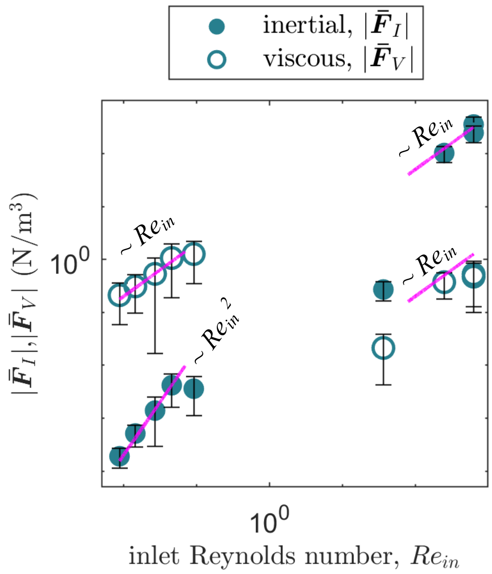

FIG. 7. Mean fluid forces (inertial $|\bar{\boldsymbol{F}}_I|$ (filled circles) and viscous $|\bar{\boldsymbol{F}}_V|$ (empty circles)) as a function of Re_{in}, at a dimensionless time of $t^* = 0.5$. The error bars represent one standard deviation from the mean (across the full 2D fracture profile). Lines indicate the power law scaling (linear or quadratic) of the forces with respect to Re_{in}.

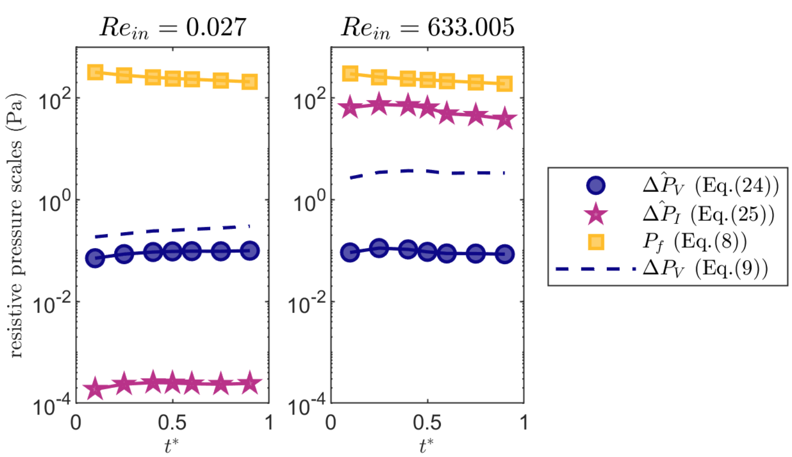

FIG. 8. Resistive pressure scales against dimensionless time t^*, for representative experiments S3 ($Re_{in} = 0.027$) and W4 ($Re_{in} = 633.005$). Numerical approximations of viscous $\Delta\hat{P}_V$ and inertial $\Delta\hat{P}_I$ pressure drops are depicted by blue circles and pink stars respectively. The fracture P_f is shown by yellow squares, and the blue dashed line represents the viscous pressure scale derived from lubrication theory (ΔP_V).

V. DISCUSSION

A. Self-similar flow in flux-driven fractures: central jet and recirculating zones

Our experiments show that a central, localized jet and recirculating flow are consistent features of Newtonian, flux-driven fractures for a wide range of inlet Reynolds numbers ($0.009 \leq Re_{in} \leq 633$) and internal flow velocities ($0.3 \leq u_{jet} \leq 235$ mm/s). Similar flux-driven fracture experiments to ours (injecting a Newtonian fluid into gelatine) have been shown to exhibit the same flow structure, with a narrow range of internal flow velocities ($u_{jet} \approx 5-10$ mm/s)[32,40,41]. This characteristic flow pattern also occurs in different jet flow problems, as first shown in the pioneering experiments of Zauner (1985)[65] where fluid was injected into a tank filled with the same fluid. The resultant jets increased in thickness with height due to entrainment from the outer flow (which we also observe). For low Re ($Re \approx 10$), the jet terminated at a finite distance from the injector and transitioned into regions of re-circulatory flow (also known as viscous toroidal eddies[65]). Using asymptotic analyis on jets with $Re > 1$, Schneider (1985)[66] showed that momentum flux decays with increasing distance from the injector, primarily due to convection at the interface between the jet and the outer flow (i.e. momentum within the jet is transferred the outer flow). This analysis suggested that viscous stresses do not contribute to the momentum flux decay, and showed that jet termination and re-circulatory flow is induced when the momentum flux becomes very small. Further examples of where this flow pattern occurs are inside a balloon being inflated with air[67,68], and in the 'stable, recirculatory flow' stage of cavity formation in a porous soil due to an increasing flow rate[69,70]. Here, we explain why our experiments exhibit this characteristic flow pattern.

In flux-driven fractures, fluid is injected at a higher rate than the fracture can propagate (Tab. IV). The resultant flow is a complex coupling of a jet flow and a solid-fluid boundary problem, where viscous effects are fundamental. Viscous forces are proportional to velocity gradients ((7)), so that viscous effects are always important in shear layers, even when viscosity is negligible in the main flow[71]. Shear layers comprise localized regions of rotating fluid elements, aka vorticity $\boldsymbol{\omega} = \nabla \times \boldsymbol{u}$. For a 2D flow, $\boldsymbol{\omega} = (0, 0, \omega)$ has one non-zero component:

$$\omega = \frac{\partial u_z}{\partial x} - \frac{\partial u_x}{\partial z}. \tag{30}$$

Inertial forces convect vorticity towards shearing boundary layers, whereas viscous forces act to diffuse vorticity away from these boundaries. Diffusive viscous flow at boundary layers controls the dynamics in the main flow[71].

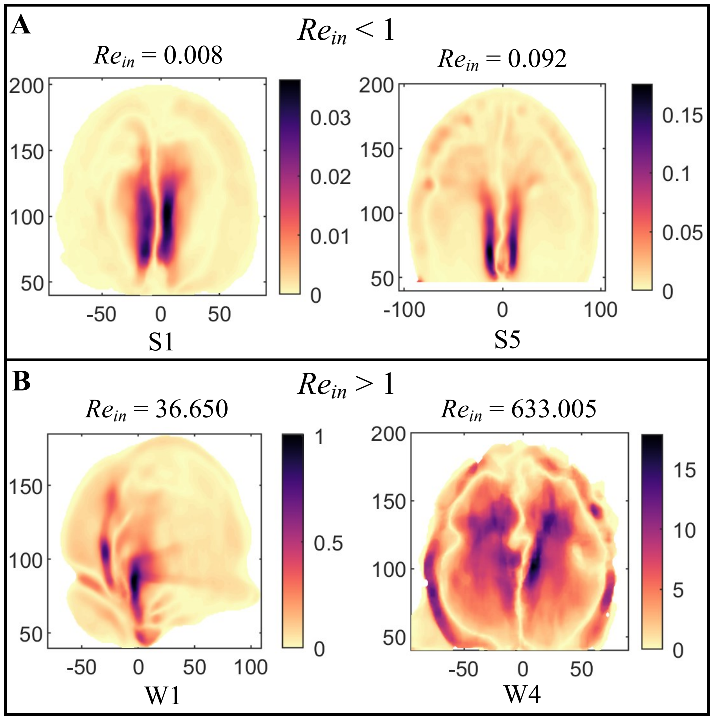

FIG. 9. Filled contours of vorticity (1/s) at a normalized time of $t^* = 0.5$ for A) low Re_{in} experiments S1 and S5 and B) high Re_{in} experiments W1 and W4. Velocity gradients were calculated according to the finite difference method[64].

In our experiments, measured velocity profiles show that there are two regions of high shear where the fluid velocity rapidly changes value: at the interface between the jet and the main flow, and the no-slip boundary (Figs. 2,3). Localized vorticity is created at the jet margins and convected with the flow, where the degree of convection depends on Re_{in} (Fig. 9). Combined with the integral no-slip condition at the solid fracture boundary[66], viscous diffusion of vorticity from the main jet leads to a recirculating vortex on either side of it. The relative strengths of convection and diffusion of vorticity vary with Re_{in}, and lead to variations of the characteristic flow pattern (see Sec. V C). In summary, the characteristic jet and recirculating flow pattern is controlled by viscous shear layers, and we propose that this is a consistent feature of Newtonian flux-driven fractures. We expect that this flow pattern is unique to flux-driven Newtonian fractures: buoyancy-driven fractures can achieve greater tip velocities and exhibit unidirectional flow profiles[41], and non-Newtonian fluids have a shear rate-dependent viscosity that would likely result in markedly different flow patterns.

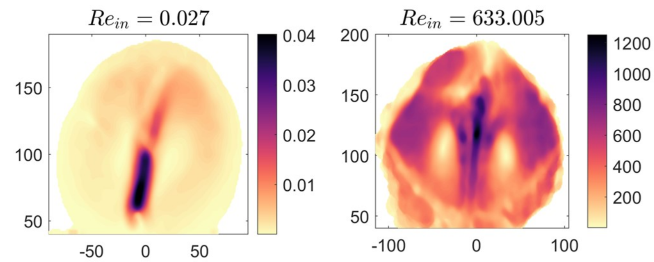

FIG. 10. Filled contours of local flow Reynolds numbers for experiments S3 ($Re_{in} = 0.027$) and W3 ($Re_{in} = 633.005$), at a normalized time of $t^* = 0.5$. Local Re values were obtained at each measurement point throughout the $2D$ fracture profile, using the local velocity magnitude $|\boldsymbol{u}|$ and constant values of ρ_f, μ and H.

B. Characteristic Reynolds numbers of fracture flow

Fluid velocity in a flux-driven fracture is strongly spatially variable, which challenges the meaning of assigning a single Reynolds number to characterize fracture flow. The Reynolds number varies locally — this is highlighted by the range in alternative Re values for a single experiment (Fig. 6), and also by profiles of local Reynolds numbers. Fig. 10 exhibits filled contours of local Re for experiments S3 ($Re_{in} < 1$) and W3 ($Re_{in} > 1$), showing the range of different flow regimes that can arize within a single fracture at a snapshot in time. In experiment S3, local Re reaches 0.04 in the jet, yet is of the order 10^{-3} throughout the majority of the profile (outside the jet). This is reflected in the alternative characteristic Re definitions (for S3), where $Re_{jet} = 0.03$ is significantly higher than $Re_{mean} = 0.004$ (Tab. III). Conversely, W4 has high local Re values throughout the fracture profile, and $Re_{jet} (\approx 845)$ is much closer in value to $Re_{mean} (\approx 440)$. Although the Re distribution is relatively uniform in W4, local Re contours also show spatial variation. Regions of both $Re > 1000$ (in the jet) and $Re < 1000$ potentially indicate simultaneous turbulent and laminar regimes.

Although Re varies locally (Fig. 10), it remains useful to characterize internal fracture flow with a single Reynolds number estimate. $Re_{mean} = \frac{\rho_f w u_{mean}}{\mu}$ characterizes the overall flow well for both $Re_{in} < 1$ and $Re_{in} > 1$. When $Re_{in} < 1$, the high-velocity (and high Re) jet region is concentrated to a relatively small area. Momentum flux near the fluid inlet is rapidly dissipated, and Re_{mean} is significantly smaller than Re_{in} and Re_{jet}. Re_{mean} is in fact approximately equal to Re_{tip} and Re_0 (Fig. 6 and Tab. III). When $Re_{in} > 1$, momentum flux is distributed throughout the fracture, and Re_{mean} is of a similar value to Re_{in} and Re_{jet}. In practical applications, u_{tip}

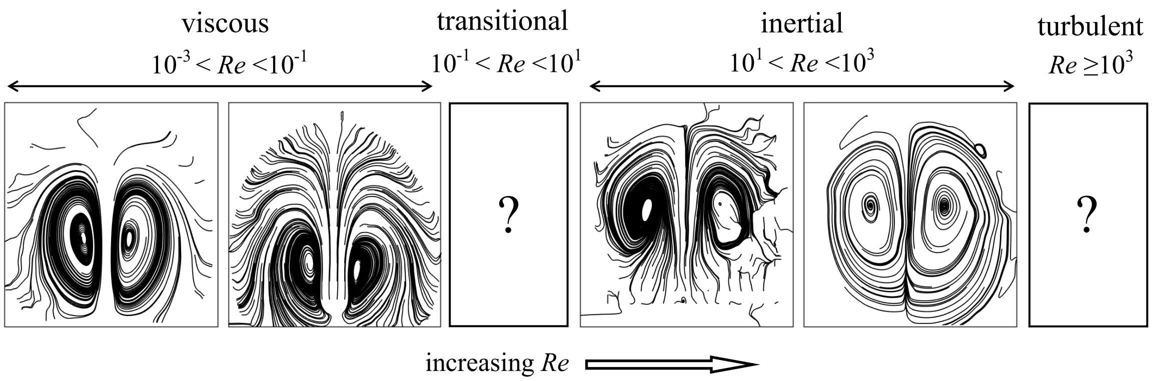

FIG. 11. Flow streamlines showing the different patterns that occur for different flow regimes (at dimensionless time $t^* = 0.5$), based on the inlet Reynolds number. From left to right, these streamlines represent experiments S1, S5, W3 and W5. Each fracture shape has been normalized by its the maximum length and breadth. Streamlines were generated using the Matlab[59] `streamlines` function.

and u_{in} can be measured[15,72,73] whereas internal fluid velocities u_{mean} and u_{jet} cannot. Therefore, we propose that Re_{tip} or Re_0 provides an appropriate characteristic Reynolds number for slow, viscosity-dominated fractures whilst Re_{in} is more appropriate for fractures with important inertial effects. Note that calculating Re_{in} also requires knowledge of the area of the injection source – this is straightforward in analogue experiments, but not necessarily in nature.

C. Flow regimes in flux-driven fractures

We propose that flux-driven fracture flow can be split into four regimes (Fig. 11) according to the inlet Reynolds number: viscous ($Re_{in} < 10^{-1}$), transitional ($10^{-1} \leq Re_{in} \leq 10^{1}$), inertial ($10^{1} < Re_{in} < 10^{3}$) and turbulent ($Re_{in} \geq 1000$)). These regimes have been identified based on internal flow patterns and the behaviour of average fluid forces across the Re_{in} range. Whilst fracture flow is characterized by a localized jet and recirculation, our experiments show that this pattern can vary significantly within the range $0.009 \leq Re_{in} \leq 633$. However, our experiments do not cover the range $0.1 \leq Re_{in} \leq 37$ — which is where we suggest a transitional regime between viscous and inertia dominated flow exists. The dynamics of flux-driven fracture flow in transitional and turbulent regimes have proved challenging to explore experimentally and therefore should be the subject of future research.

1. Viscous regime

In the viscous regime ($Re_{in} < 0.1$), the jet always terminates before reaching the vertical fracture tip. Increasing Re_{in} leads to shorter jets with higher velocities near the inlet (Figs. 2,3A), and a higher magnitude of vorticity over a smaller region (Fig. 9). Viscous diffusion of vorticity also reduces, and the recirculatory zones become smaller yet more intense (i.e. contain higher velocities and vorticity) with increasing Re_{in} (Fig. 11). A decrease in jet height with increasing Re is the opposite of what occurs for unconfined jets in a fluid tank with no upper boundary[65], for $Re > 1$. Those jets decrease in height with decreasing Re, as more momentum is dissipated by viscous forces.

Viscous forces are greater than inertial forces and scale linearly with Re_{in} initially, whilst inertial forces increase at a faster rate and scale with Re_{in}^2 (Fig. 7). This is expected from simple order of magnitude estimates of the fluid force terms (see Equations (11) and (12)), where $|\bar{\boldsymbol{F}}_V|$ scale with characteristic velocity $\mathscr{U}$ and $|\bar{\boldsymbol{F}}_I|$ scales with $\mathscr{U}^2$ (note that the Reynolds number represents a velocity scale). Higher inertial forces lead to higher velocities and vorticity in the jet, yet the simultaneous increase in viscous forces inhibits the jet from increasing in length. As Re_{in} approaches unity, the increase in both $|\bar{\boldsymbol{F}}_I|$ and $|\bar{\boldsymbol{F}}_V|$ slows down, indicating that the flow is near the onset of the transitional regime.

2. Inertial regime

For $10^1 < Re_{in} < 10^3$, the jets do not terminate prior to reaching the upper solid boundary (Fig. 3A). Vorticity is convected with the jet flow and along the fracture margins (Fig. 9). For the highest $Re_{in} = 633$ (experiments W3 and W4), convection of vorticity towards the solid boundary dominates over viscous diffusion away from it, and a layer of high vorticity is confined to the entire fracture boundary. This leads to flow circulation throughout the entire fracture. With decreasing Re_{in}, vorticity is convected some distance along the upper fracture boundary before the flow loses momentum and vorticity is diffused from the boundary into the main flow. This results in vortices that are located closer to the upper fracture tip (as opposed to $Re_{in} < 1$ where the vortices are located near the injector Fig. 11). Based on numerical simulations of an air-inflated balloon, it is expected that at higher Re, each vortex will split into multiple smaller scale vortices[68]. However, this pattern would be altered significantly by turbulent flow.

Scaling arguments (see Equations (11) and (12)) suggest that $|\bar{\boldsymbol{F}}_I|$ should increase with the square of the velocity (and therefore the Reynolds number). Whilst this is observed within the viscous regime, when $Re_{in} > 1$ inertial forces increase linearly with Re_{in} (Fig 7). Unlike in the viscous regime where velocities vary smoothly over larger length scales (Fig. 3), in the inertial regime, flow is strongly spatially variable with finer-scale flow structures. Therefore, an average approximation of the inertial force may not be fully representative. Our results suggest that as Re_{in} decrease and approaches one, $|\bar{\boldsymbol{F}}_I|$ and $|\bar{\boldsymbol{F}}_V|$ deviate from their scaling laws. This potentially indicates that the flow is near the transitional regime, at the higher end of the Re_{in} range.

3. Transitional regime

Our experiments do not span the transitional range $0.1 \leq Re_{in} \leq 36$, which is challenging to achieve experimentally. When injecting silicone oil ($Re_{in} < 0.1$), we reached the maximum possible Re_{in} $(= 0.092)$ that could be achieved experimentally. For the water experiments, it was not possible to inject fluid at a lower rate than presented here, without potential settling of the tracer particles. Therefore it is currently unclear how internal fracture flow behaves in the transition from viscous to inertial flow. However, the flow behaviour in the viscous and inertial regimes gives some insight into what occurs during the transition.

Fracture tip velocities are very similar for experiments that lie at the transitional margins, which suggests that the transitional regime has a narrow range in tip velocities (Fig. 12). This region of approximately constant tip velocity coincides with a shift in the behaviour of the fluid forces (Fig.7). Unlike in the viscous and inertial regimes $|\bar{\boldsymbol{F}}_V|$ and $|\bar{\boldsymbol{F}}_I|$ do not appear to be a simple function of Re_{in}. During the transition from viscous to inertial flow, $|\bar{\boldsymbol{F}}_V|$ must decrease from the high values in the $Re_{in} < 1$ experiments to the lowest values in the $Re_{in} > 1$ experiments. Similarly, $|\bar{\boldsymbol{F}}_I|$ must increase across the transition, although Fig.7 indicates that this increase is non-linear and $|\bar{\boldsymbol{F}}_I|$ potentially plateaus before increasing again. However, there are not enough data points to determine how the fluid forces evolve across the transitional regime. When $Re \approx 1$, inertial and viscous forces become similar in magnitude and are of equal importance. More experiments are needed to understand how fluid forces evolve across the transitional regime, and determine the exact Re values at which the transition occurs. Future experiments could use tracer particles with a lower density, or a Newtonian fluid with a higher density and viscosity than water (yet less viscous than silicone oil).

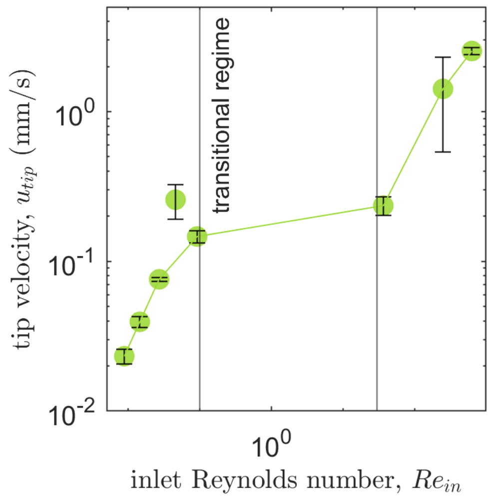

FIG. 12. Vertical fracture tip velocity u_{tip} (mm/s) against Re_{in} at a dimensionless time of $t^* = 0.5$. The line connects all experiments except S4, which is an outlier due to a trapped bubble and additional buoyancy effects.

4. Turbulent regime

The onset of turbulence in fractures is commonly assumed to occur at $Re \approx 1000$[1,3,74]. Experiments W3 and W4 have regions of flow with both local $Re > 1000$ and $Re < 1000$ (Fig.10), potentially indicating simultaneous laminar and turbulent regimes. However, the uniform structure of the jet (Fig. 4 in the Supplementary Material) and consistent, non-chaotic flow behavior suggest that fracture flow is not turbulent in our experiments[75]. We injected fluid at the fastest rate achievable with our injection equipment, yet could not achieve turbulence when injecting water. Note that, it could be possible to achieve turbulence by injecting liquids with a lower viscosity than water, yet these liquids also needs to satisfy the condition of having a similar density to gelatine and being able to hold tracer particles in suspension. An appropriate liquid may be challenging to identify, and this could be explored in future work. Thus, the dynamics of turbulent fracture flow remain an open question. Local Re contours (Fig.10) suggest that the central jet would be the first region of flow to become turbulent, but it is currently unclear whether the characteristic circulating flow structure would persist at higher Reynolds numbers. Note that 2D flow profiles do not reveal how the fluid is behaving in the third out-of-plane dimension — 3D imaging is required to know if the flow is chaotic across the fracture thickness.

D. Controls on fracture propagation

Pressure scale estimates (Fig 8) suggest that the initial deceleration in u_{tip} is due to an increase in either the viscous or inertial resistive pressure as the fracture grows, depending on Re_{in}. The resistance to fracture (characterized by P_f) decreases with fracture length, causing the fracture to accelerate towards the free surface[76]. The horizontal fracture growth, u_W consistently decelerates, which doesn't coincide with any pressure scale. However, this does coincide with a decrease in the circulation velocity over time (Fig. 5H), suggesting that a reduction in the downwards flow velocity leads to a reduction in u_W.

The tip velocity u_{tip} is a linear function of the flux Q (Fig. 4), yet for a given tip velocity, there is a wide range of potential fluid behavior within. Across the transitional regime, injection rates and tip velocities are very similar, yet Re_{in} ranges from approximately 0.1 to 30 (Fig. 12). This suggests that a constant proportion of the driving pressure (due to fluid injection) contributes towards fracture propagation, regardless of the internal fluid behavior. The remainder of this applied pressure is distributed via different combinations of the inertial and fluid forces (Fig. 8), producing different internal flow patterns (Figs.2 and 11). Although the fluid injection rate controls fracture propagation, we expect that the internal fluid dynamics have a subtle but potentially significant effect on the coupled solid host deformation. Further experiments focusing on solid displacement measurements are needed to investigate this.

Through a theoretical analysis of a 2D flux-driven fracture propagating in an infinite, elastic medium, Emerman et al. (1986)[10] found the tip velocity to be a linear function of the inlet velocity, with $u_{tip} \approx 0.45 u_{in}$. This is a markedly different relationship to our experiments, where u_{tip} is consistently less than 1% of u_{in} (Fig. 2 in the Supplementary Material). This difference is likely due to the 2D plane-strain model assumption with an infinite fracture width, as opposed to the point source injection method in our experiments. In propagating, non-buoyant fractures, the fracture width is always expected to exceed the length scale of the fluid inlet due to radial fracture growth. However, the size of the injection area affects the inlet Reynolds number and will have a strong effect on flow dynamics. This was investigated in numerical simulations of the flow within an inflating balloon[68]: smaller inlets led to longer and more focused jets, yet jet formation and flow circulation always occurred. Future experimental work could investigate the effect of the fluid inlet area on flux-driven fracture dynamics.

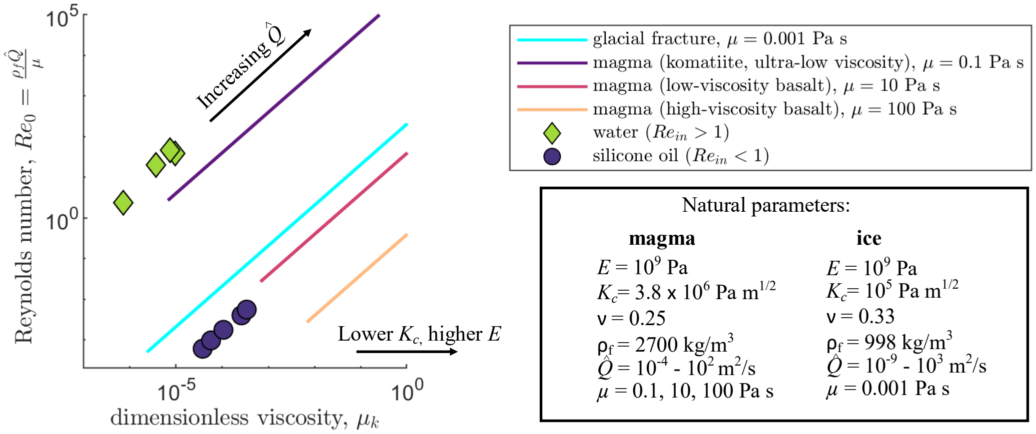

FIG. 13. Dimensionless parameter space for experiments and natural geophysical examples, defined by the dimensionless viscosity μ_k and the Reynolds number $Re_0 = \frac{\hat{Q}\rho_f}{\mu}$. The water and silicone oil experiments are depicted by green diamonds and purple circles respectively. Each line represents the potential range of μ_k and Re_0 for a range of $\hat{Q} = Q/W$ values, with all other parameters constant. The light blue line depicts ice fractures, whilst the pink and purple lines represent dykes with for three different magma viscosities.

E. Application to magmatic and glacial systems

Experimental, flux-driven fractures in gelatine are an idealized analogue of natural, geophysical flux-driven fractures. The dimensionless viscosity μ_k and inertia R_k are $\ll 1$ (Tab. IV), confirming that the analogue fractures propagate in the toughness regime. Although fracture toughness dominates overall, the ratio of viscous and inertial forces varies significantly across the experiments. We now consider the dynamic similarity between the analogue experiments and natural glacial and magmatic systems by comparing the dimensionless parameter space defined by μ_k and the Reynolds number. For the latter, we use the definition $Re_0 = \frac{\rho_f \hat{Q}}{\mu}$, where $\hat{Q} = \frac{Q}{W}$ is the flux per unit width, in order to directly compare with nature. This requires appropriate estimates of magmatic and glacial parameters.

The applicability of the experiments to natural systems is limited by the model assumptions (e.g. elastic solid, Newtonian fluid). Glacial ice is not strictly linear elastic, but it is accepted to behave in an elastic way under fracture[77]. In magmatic systems the assumption of elasticity is only applicable to the lithosphere[78]. Appropriate E values range from $10^8 - 10^{10}$ Pa for glaciers[79] and $10^9 - 10^{10}$ Pa for the elastic crust[80]. Water in glacial crevasses is Newtonian ($\mu \approx 10^{-3}$ Pa s), whereas the rheology of magma depends on the relative proportions of crystals, melt and bubbles[81]. Newtonian magmas are relatively crystal-poor with no bubbles, representing a primitive mafic (low-silica) magma: μ ranges from $10^1 - 10^2$ Pa s for basaltic magma[82,83], yet can be as low as 10^{-2} for ultramafic magmas such as komatiite or carbonatite[29]. Numerical models of basaltic dykes with a constant flux suggest that Q can range from $1 - 1000$ m^3/s[84], whereas glacial fractures exhibit a wider range of Q values — from $O(10^{-5})$ m^3/s in thin fracture networks[73], to $O(10^3)$ m^3/s in rapid drainage events[15]. Fracture lengths, widths and thicknesses have a wide variety of potential values, and we consider a range of fracture sizes. The natural parameter estimates are summarized in Tab. IV.

According to the dimensionless parameter space defined by μ_k and Re_0 (Fig. 13), our experiments represent the lowest end of the μ_k spectrum for natural magmatic and glacial fractures. The natural parameter space is depicted as a series of linear lines, each representing a different fluid viscosity, and a wide range of $\hat{Q}$ values. All other parameters are assumed to be constant: whilst ρ_f and ν have little effect on the overall parameter space, E and K_C do act to shift the dimensionless viscosity range significantly. Here we have selected values that best represent the experiments in this parameter space, whilst being in the valid range specified above (the upper and lower ends of the E and K_C ranges respectively, see Fig. 13 inset box). Both sets of experiments represent natural injections with a low flux (per unit width). Recall that the rate of injection is limited by the fluid viscosity (silicone oil could not be injected at a higher rate than achieved here). The silicone oil experiments ($Re_{in} < 1$) are fairly well representative of glacial fractures and basaltic dykes, whereas the water experiments ($Re_{in} > 1$) are more representative of a very low viscosity magma, such as a primitive komatiite. Future work could explore fractures with higher μ_k, and fill in the gaps in our understanding of flux-driven fluid dynamics across the natural parameter space. A higher μ_k could be achieved by using other fluids with different viscosities, and injecting them at a range of rates.

VI. CONCLUSIONS

Analague experiments of flux-driven fractures have shown that internal fracture flow has a self-similar pattern of a high-velocity central jet with a zone of fluid recirculation on either side, consistent across a range of regimes. We have utilized PIV velocity data to identify four potential regimes: viscous, inertial, transitional, and turbulent. Viscous and inertial regimes were produced experimentally (with some experiments perhaps bordering the transitional regime) for

	Experiments	Magma (basalt)	Ice
E	2278 - 4337	$1\times10^9 - 10^{10}$[a]	$10^8 - 10^{10}$[i]
K_C	66-93	$1.4\times10^6 - 3.8\times10^6$[b]	$10^5 - 20^5$[j,k]
ν	0.5	0.1-0.5[a]	0.3[i]
Q	4.4×10^{-8} - 7.0×10^{-6}	1-10^3[c]	$10^{-5} - 10^3$[l,m]
μ	0.001 - 0.45	10^1-10^3[d,e]	10^{-3}[g]
ρ_f	998,1040	2700[p]	998[g]
H	0.003 - 0.015	0.1 - 10[d,f]	$10^{-3} - 1$[n]
W	$0.14 - 0.18$[o]	$10^1 - 10^4$[h]	$1 - 10^4$[h]
Re_0	$6\times10^{-4} - 5\times10^1$	$10^{-4} - 10^4$	$10^{-4} - 10^8$
μ_k	$5\times10^{-7} - 3\times10^{-4}$	$10^{-5} - 10^{10}$	$10^{-8} - 10^{10}$
R_k	$4\times10^{-10} - 9\times10^{-6}$	-	-

TABLE IV. Characteristic parameters of flux-driven fractures in the current experiments and magmatic and glacial settings: Young's modulus E (Pa), fracture toughness K_C (Pa m$^{\frac{1}{2}}$), Poisson's ratio ν (dimensionless), volumetric flux Q (m^3/s), viscosity μ (Pa s), fluid density ρ_f (kg/m^3), fracture thickness H (m), fracture width W (m), Reynolds number $Re_0 = \frac{Q\rho_f}{B\mu}$, dimensionless viscosity $\mu_k = \frac{12\mu Q'}{E'}\left(\frac{E'}{K'}\right)^4$, dimensionless inertia $R_k = \frac{\rho_f E'^{5/3} Q'^{5/3}}{K'^{8/3} t^{1/3}}$. R_k was calculated at $t^* = 0.5$ for the experiments, and not estimated in nature. References for natural values: a) Heap et al. (2020)[80], b) Balme et al. (2004)[85], c) Traversa et al. (2010)[84], d) Wada et al. (1994)[82], e) Roman et al. (2021)[83], f) Rubin (1995)[3], g) values for water, h) assuming a range of sizes, i) Vaughan (1995)[79], j) Fischer et al. (1995)[86], k) Rist et al. (1999)[87], l) Das et al. (2008)[15], m) Fountain et al. (2005)[73], n) Holdsworth et al. (1969)[88], o) range in experimental values at $t^* = 0.5$, p) typical basalt value[89].

inlet Reynolds numbers spanning $O(10^{-3}) \le Re_{in} \le O(10^3)$. In the viscous regime, the jet and adjacent vortices shrink with increasing Re yet become more intensely localized near the jet. To our knowledge, this is the first experimental insight into the behavior of jets at $Re < 1$. In the inertial regime, the jet length always exceeds the fracture length, and an increase in Re_{in} leads to a greater degree of flow circulation. Although data are lacking for the transitional regime ($Re \approx 1$) due to experimental limitations, we propose that the average fluid forces have a complex relationship with Re_{in}, yet fractures propagate at similar tip velocities within this regime. Despite the complexity of the internal flow, the propagation velocity is a linear function of the flux Q. These results have important implications for interpreting natural data on propagating fractures, and developing better numerical models to predict them. A key advantage of our experimental model is that the solid transparency allows for measurements of fracture and flow dynamics in real-time. Furthermore, the model scales appropriately with natural flux-driven fractures, as shown by the dimensionless parameter space defined by Re and the dimensionless viscosity μ_k. However, there remains a knowledge gap regarding transitional and turbulent flow in fractures. Model simplifications also restrict our analysis to fractures in elastic solids injected by Newtonian fluids with a constant viscosity and density. These assumptions are most restrictive in the application to volcanology, where hot rocks can deform inelastically, and crystal and bubble content can lead to variations in magma viscosity and density. Future experiments (using different fluid and solid properties) are required to understand the complete range of flow regimes in flux-driven fractures, across the full natural parameter space. Experimental measurements in 3D would bring further advancement to our understanding of fracture dynamics.

VII. SUPPLEMENTARY MATERIAL

Supplementary Material to this article is provided online, containing further details on the experimental methodology and additional results visualizations.

ACKNOWLEDGMENTS

The authors thank Alex Charogiannis at LaVision for advice and assistance with the data collection and processing. David Dennis is thanked for guidance on the laser imaging setup and apparatus design. Kate Williams, Amanda Valentine-Baars, Zak Derler, Dawid Rybak, Matìas Clunes and Sam Poppe are thanked for their assistance in the laboratory. James Lea, Tom Chudley and David McNamara are thanked for their input on the applicability of these experiments to natural systems (through discussions at a workshop funded by a NERC Cross-Disciplinary Research for Environmental Sciences Discovery grant). Henry Ng is thanked for his advice regarding data processing. CC thanks Fryderyk Wilczynski for helpful talks about complex fluid dynamics. JK thanks Thomas Jones for early discussions regarding the importance of Reynolds numbers in volcanology. The authors thank two anonymous reviewers and the editor for their thoughtful comments which improved the manuscript. This work was funded by UKRI Future Leaders Fellowship (MR/S035141/1) awarded to JK.

DATA AVAILABILITY STATEMENT

The data that support the findings of this study are openly available in the NERC EDS National Geoscience Data Centre at `https://doi.org/10.5285/92383dba-8b6e-43da-9d78-e8784b97124c`.

Appendix A: Nomenclature

	Experimental parameters
A	fluid inlet area
c_g	gelatine concentration
d	fluid inlet diameter
E	Young's modulus
K_C	fracture toughness
μ	dynamic viscosity
ν	Poisson's ratio
ρ_f	fluid density
Q	volumetric flux
$\hat{Q}$	flux per unit width
t_0	time when $L = 10$ cm
t_{erupt}	time between t_0 and eruption
u_{in}	inlet velocity
	Geometry
H	fracture thickness
L	fracture length
W	fracture width
x	horizontal axis
y	out of plane axis
z	vertical axis
$\hat{x}$	normalized horizontal coordinate
$\hat{z}$	normalized vertical coordinate
$\hat{z}_{max}$	normalized height of velocity maximum

	Mathematical formulation
$\partial/\partial t$	partial time derivative
∇^2	Laplace operator
$\boldsymbol{F}_I$	inertial force, $\boldsymbol{F}_I = (F_{Ix}, F_{Iz})$
$\boldsymbol{F}_V$	viscous force, $\boldsymbol{F}_V = (F_{Vx}, F_{Vz})$
$\boldsymbol{n}$	unit normal
p	dynamic pressure
P_F	fracture pressure scale
ΔP_V	viscous pressure scale
ΔP_I	inertial pressure scale
t	time, $t_0 \leq t \leq t_{max}$
$\boldsymbol{u}$	velocity vector, $\boldsymbol{u} = (u_x, u_z)$
$\boldsymbol{\omega}$	vorticity, $\boldsymbol{\omega} = \nabla \times \boldsymbol{u}$
ω	vorticity magnitude
	Characteristic velocities
u_{in}	inlet velocity
u_{tip}	vertical tip velocity
u_{tip50}	vertical tip velocity when $t^* = 0.5$
u_W	horizontal tip velocity
u_{W50}	horizontal tip velocity when $t^* = 0.5$
u_{mean}	mean absolute velocity
u_{down}	representative downwards (downflow) velocity
u_{circ}	circulation velocity
u_{jet}	jet velocity
	PIV analysis
r_c	correlation value
Δt	time increment
τ_r	particle relaxation time
U_g	Stokes particle velocity
Δx	grid spacing

	Dimensionless numbers
μ_k	dimensionless viscosity
Re_0	flux Reynolds number
Re_{in}	inlet Reynolds number
Re_{mean}	mean Reynolds number
Re_{jet}	jet Reynolds number
Re_{tip}	tip Reynolds number
R_k	dimensionless inertia
St	Stokes number
t^*	dimensionless time, $t^* = (t - t_0)/t_{erupt}$
	Numerical (finite difference) approximations
$\hat{\boldsymbol{F}}_I$	inertial force
$\hat{\boldsymbol{F}}_V$	viscous force
$\bar{\boldsymbol{F}}_I$	average inertial force
$\bar{\boldsymbol{F}}_V$	average viscous force
$\Delta\hat{P}_V$	viscous pressure scale
$\Delta\hat{P}_I$	inertial pressure scale

REFERENCES

[1]D. L. Spence, D. A. and Turcotte, "Magma-Driven Propagation of Cracks," **90**, 575–580 (1985).

[2]J. R. Lister and R. C. Kerr, "Fluid-mechanical models of crack propagation and their application to magma transport in dykes," Journal of Geophysical Research: Solid Earth **96**, 10049–10077 (1991).

[3]A. M. Rubin, "Propagation of Magma-Filled Cracks," Annual Review of Earth and Planetary Sciences **23**, 287–336 (1995).

[4]A. G. Fountain and J. S. Walder, "Water flow through temperate glaciers," Reviews of Geophysics **36**, 299–328 (1998).

[5]V. C. Tsai and J. R. Rice, "A model for turbulent hydraulic fracture and application to crack propagation at glacier beds," Journal of Geophysical Research: Earth Surface **115** (2010).

[6]D. M. Chandler and A. Hubbard, "Widespread partial-depth hydrofractures in ice sheets driven by supraglacial streams," Nature Geoscience , 1–7 (2023).

[7]P. Olasolo, M. Juárez, M. Morales, I. Liarte, *et al.*, "Enhanced geothermal systems (egs): A review," Renewable and Sustainable Energy Reviews **56**, 133–144 (2016).

[8]T. Guo, F. Gong, X. Wang, Q. Lin, Z. Qu, and W. Zhang, "Performance of enhanced geothermal system (egs) in fractured geothermal reservoirs with co2 as working fluid," Applied thermal engineering **152**, 215–230 (2019).

[9]W. Kumari and P. Ranjith, "Sustainable development of enhanced geothermal systems based on geotechnical research–a review," Earth-Science Reviews **199**, 102955 (2019).

[10]S. H. Emerman, D. L. Turcotte, and D. A. Spence, "Transport of magma and hydrothermal solutions by laminar and turbulent fluid fracture," Physics of the Earth and Planetary Interiors **41**, 249–259 (1986).

[11]S. R. Sparks, H. Sigurdsson, and L. Wilson, "Magma mixing: a mechanism for triggering acid explosive eruptions," Nature **267**, 315–318 (1977).

[12]T. J. Jones and E. W. Llewellin, "Convective tipping point initiates localization of basaltic fissure eruptions," Earth and Planetary Science Letters **1**, 116637 (2020).

[13]P. Christoffersen, M. Bougamont, A. Hubbard, S. H. Doyle, S. Grigsby, and R. Pettersson, "Cascading lake drainage on the greenland ice sheet triggered by tensile shock and fracture," Nature Communications **9**, 1064 (2018).

[14] C. J. van der Veen, "Fracture propagation as means of rapidly transferring surface meltwater to the base of glaciers," Geophysical Research Letters **34**, 1–5 (2007).

[15] S. B. Das, I. Joughin, M. D. Behn, I. M. Howat, M. A. King, D. Lizarralde, and M. P. Bhatia, "Fracture propagation to the base of the greenland ice sheet during supraglacial lake drainage," Science **320**, 778–781 (2008).

[16] D. Stevenson, "Migration of fluid-filled cracks: Applications to terrestrial and icy bodies," in *Lunar and Planetary Science*, Vol. 13 (1982) pp. 768–769.

[17] E. Rivalta, B. Taisne, A. Bunger, and R. Katz, "A review of mechanical models of dike propagation: Schools of thought, results and future directions," Tectonophysics **638**, 1–42 (2015).

[18] S. Furst, F. Maccaferri, and V. Pinel, "Modeling the shape and velocity of magmatic intrusions, a new numerical approach," Journal of Geophysical Research: Solid Earth , 1–24 (2023).

[19] E. Rivalta, F. Corbi, L. Passarelli, V. Acocella, T. Davis, and M. A. Di Vito, "Stress inversions to forecast magma pathways and eruptive vent location," Science advances **5**, eaau9784 (2019).

[20] T. Davis, E. Rivalta, D. Smittarello, and R. F. Katz, "Ascent rates of 3-d fractures driven by a finite batch of buoyant fluid," Journal of Fluid Mechanics **954**, A12 (2023).

[21] E. Detournay, "Mechanics of Hydraulic Fractures," Annual Review of Fluid Mechanics **48**, 311–339 (2016).

[22] F. Galetto, A. Bonaccorso, and V. Acocella, "Relating dike geometry and injection rate in analogue flux-driven experiments," Frontiers in Earth Science **9**, 665865 (2021).

[23] S. Roper and J. Lister, "Buoyancy-driven crack propagation: the limit of large fracture toughness," Journal of Fluid Mechanics **580**, 359–380 (2007).

[24] R. B. Alley, T. K. Dupont, B. R. Parizek, and S. Anandakrishnan, "Access of surface meltwater to beds of sub-freezing glaciers: preliminary insights," Annals of Glaciology **40**, 8–14 (2005).

[25] B. Taisne and C. Jaupart, "Dike propagation through layered rocks," Journal of Geophysical Research: Solid Earth **114** (2009), 10.1029/2008JB006228.

[26] N. C. Huang, A. A. Szewczyk, and Y. C. Li, "Self-Similar Solution in Problems of Hydraulic Fracturing," Journal of Applied Mechanics **57**, 877–881 (1990).

[27] D. I. Garagash, "Plane-strain propagation of a fluid-driven fracture during injection and shut-in: Asymptotics of large toughness," Engineering Fracture Mechanics **73**, 456–481 (2006).

[28] H. Zia and B. Lecampion, "Propagation of a height contained hydraulic fracture in turbulent flow regimes," International Journal of Solids and Structures **110-111**, 265–278 (2017).

[29]C. E. Lesher and F. J. Spera, "Thermodynamic and transport properties of silicate melts and magma," in *The encyclopedia of volcanoes* (Elsevier, 2015) pp. 113–141.

[30]A. F. Glazner, "Magmatic life at low reynolds number," Geology **42**, 935–938 (2014).

[31]K. Xue, Z. Zhang, S. Hao, P. Luo, and Y. Wang, "On the onset of nonlinear fluid flow transition in rock fracture network: Theoretical and computational fluid dynamic investigation," Physics of Fluids **34** (2022).

[32]J. L. Kavanagh, A. J. Burns, S. Hilmi Hazim, E. P. Wood, S. A. Martin, S. Hignett, and D. J. Dennis, "Challenging dyke ascent models using novel laboratory experiments: Implications for reinterpreting evidence of magma ascent and volcanism," Journal of Volcanology and Geothermal Research **354**, 87–101 (2018).

[33]J. L. Kavanagh, S. L. Engwell, and S. A. Martin, "A review of laboratory and numerical modelling in volcanology," Solid Earth **9**, 531–571 (2018).

[34]S. Urbani, V. Acocella, and E. Rivalta, "What drives the lateral versus vertical propagation of dikes? insights from analogue models," Journal of Geophysical Research: Solid Earth **123**, 3680–3697 (2018).

[35]A. Takada, "Experimental study on propagation of liquid-filled crack in gelatin: Shape and velocity in hydrostatic stress condition," Journal of Geophysical Research: Solid Earth **95**, 8471–8481 (1990).

[36]T. Dahm, "On the shape and velocity of fluid-filled fractures in the Earth," Geophysical Journal International **142**, 181–192 (2000).

[37]T. Menand and S. R. Tait, "The propagation of a buoyant liquid-filled fissure from a source under constant pressure: An experimental approach," Journal of Geophysical Research: Solid Earth **107**, ECV 16–1–ECV 16–14 (2002).

[38]E. Rivalta, M. Böttinger, and T. Dahm, "Buoyancy-driven fracture ascent: Experiments in layered gelatine," Journal of Volcanology and Geothermal Research **144**, 273–285 (2005).

[39]S. Pansino, A. Emadzadeh, and B. Taisne, "Modeling dike propagation in both vertical length and horizontal breadth," Journal of Geophysical Research: Solid Earth **127**, e2022JB024593 (2022).

[40]K. Williams, J. Kavanagh, and D. Dennis, "Focused flow during the formation and propagation of sills: Insights from analogue experiments," Earth and Planetary Science Letters **584**, 117492 (2022).

[41]S. Pansino, A. Emadzadeh, and B. Taisne, "Magma Flow Patterns in Dikes: Observations From Analogue Experiments," Journal of Geophysical Research: Solid Earth **128** (2023), 10.1029/2022jb025463.

[42]B. Lawn, *Fracture of Brittle Solids*, 2nd ed. (Cambridge University Press, 1993).

[43]J. R. Lister, "Buoyancy-driven fluid fracture: the effects of material toughness and of low-viscosity precursors," Journal of Fluid Mechanics **210**, 263–280 (1990).

[44]B. Taisne, S. Tait, and C. Jaupart, "Conditions for the arrest of a vertical propagating dyke," Bulletin of Volcanology **73**, 191–204 (2011).

[45]R. W. Zimmerman, A. Al-Yaarubi, C. C. Pain, and C. A. Grattoni, "Non-linear regimes of fluid flow in rock fractures," International Journal of Rock Mechanics and Mining Sciences **41**, 163–169 (2004).

[46]E. Dontsov, "Tip region of a hydraulic fracture driven by a laminar-to-turbulent fluid flow," Journal of Fluid Mechanics **797**, R2 (2016).

[47]R. Patel, J. Browning, D. S. Sarma, and A. Panda, "Mechanical fragmentation and thermal erosion of dyke adjacent host rocks induced by fluid-dynamic shear stress and latent heat release in response to turbulent magma flow," Journal of Volcanology and Geothermal Research **429**, 107599 (2022).

[48]D. J. Acheson, "Elementary fluid dynamics," (Oxford University Press, Oxford, 1990) Section 1, pp. 260–299, 1st ed.

[49]L. Wilson, R. S. J. Sparks, and G. P. Walker, "Explosive volcanic eruptions—iv. the control of magma properties and conduit geometry on eruption column behaviour," Geophysical Journal International **63**, 117–148 (1980).

[50]*DaVis 10.2 Software*, LaVision GmbH, Gottingen, Germany, 10th ed. (2022).

[51]*FlowMaster Getting Started*, LaVision GmbH, Gottingen, Germany, 10th ed. (2021).

[52]J. L. Kavanagh, T. Menand, and K. A. Daniels, "Gelatine as a crustal analogue: Determining elastic properties for modelling magmatic intrusions," Tectonophysics **582**, 101–111 (2013).

[53]R. J. Adrian and J. Westerweel, *Particle image velocimetry*, 30 (Cambridge university press, 2011).

[54]M. Tischer, M. I. Bursik, and E. B. Pitman, "Kinematics of sand avalanches using particle-image velocimetry," Journal of Sedimentary Research **71**, 355–364 (2001).

[55]C. R. Marshall, R. M. Dorrell, G. M. Keevil, J. Peakall, and S. M. Tobias, "Observations of large-scale coherent structures in gravity currents: implications for flow dynamics," Experiments

in Fluids **62**, 1–18 (2021).

[56]C. M. Chalk, J. Peakall, G. Keevil, and R. Fuentes, "Spatial and temporal evolution of an experimental debris flow, exhibiting coupled fluid and particulate phases," Acta Geotechnica **17**, 965–979 (2022).

[57]A. Rosenthal, K. Lüdemann, and A. Tilgner, "Staircase formation in unstably stratified double diffusive finger convection," Physics of Fluids **34** (2022).

[58]Y. Liu and H. M. Fritz, "Physical modeling of spikes during the volcanic tsunami generation," Physics of Fluids **35** (2023).

[59]*MATLAB version 9.13.0.1967605 (R2022b) Prerelease*, The Mathworks, Inc., Natick, Massachusetts (2022).

[60]C. M. Chalk and J. L. Kavanagh, "Spatial and temporal datasets for 11 different small-scale laboratory experiments of fluid-driven fractures." `https://doi.org/10.5285/92383dba-8b6e-43da-9d78-e8784b97124c` (2024), NERC EDS National Geoscience Data Centre. (Dataset).

[61]*MATLAB and Image Processing Toolbox Release 2022b*, The Mathworks, Inc., Natick, Massachusetts (2022).

[62]*MATLAB and Statistics and Machine Learning Toolbox Release 2022b*, The Mathworks, Inc., Natick, Massachusetts (2022).

[63]O. Gal, "fitellipse," (2023).

[64]J. W. Thomas, *Numerical Partial Differential Equations: Finite Difference Methods*, 1st ed. (Springer New York, NY, 1995).

[65]E. Zauner, "Visualization of the viscous flow induced by a round jet," Journal of Fluid Mechanics **154**, 111–119 (1985).

[66]W. Schneider, "Decay of momentum flux in submerged jets," Journal of Fluid Mechanics **154**, 91–110 (1985).

[67]Y. Bazilevs, M. Hsu, J. Kiendl, R. Wüchner, and K. Bletzinger, "3D Simulation of Wind Turbine Rotors at Full Scale. Part II: Fluid – Structure Interaction Modeling with Composite Blades," International Journal for Numerical Methods in Fluids **65**, 236–253 (2011).

[68]D. Ilssar and A. D. Gat, "On the inflation and deflation dynamics of liquid-filled, hyperelastic balloons," Journal of Fluids and Structures **94**, 102936 (2020), arXiv:1908.04074.

[69]Y. Tang, D. H. Chan, and D. Z. Zhu, "Numerical investigation of sand-bed erosion by an upward water jet," Journal of Engineering Mechanics **143**, 04017104 (2017).

[70] H. E. Schulz, J. E. van Zyl, T. Yu, I. E. L. Neto, F. A. Filho, N. A. Correa, I. M. Benites, and H. Wang, "Hydraulics of fluidized cavities in porous matrices: cavity heights and stability for upward water jets," Journal of Hydraulic Engineering **147**, 04021037 (2021).

[71] D. J. Acheson, "Elementary fluid dynamics," (Oxford University Press, Oxford, 1990) Section 8, pp. 260–299, 1st ed.

[72] J. Battaglia, V. Ferrazzini, T. Staudacher, K. Aki, and J.-L. Cheminée, "Pre-eruptive migration of earthquakes at the piton de la fournaise volcano (réunion island)," Geophysical Journal International **161**, 549–558 (2005).

[73] A. G. Fountain, R. W. Jacobel, R. Schlichting, and P. Jansson, "Fractures as the main pathways of water flow in temperate glaciers," Nature **433**, 618–621 (2005).

[74] T. Watanabe, T. Masuyama, K. Nagaoka, and T. Tahara, "Analog experiments on magma-filled cracks," Earth, planets and space **54**, 1247–1261 (2002).

[75] P. O'Neill, J. Soria, and D. Honnery, "The stability of low reynolds number round jets," Experiments in fluids **36**, 473–483 (2004).

[76] E. Rivalta and T. Dahm, "Acceleration of buoyancy-driven fractures and magmatic dikes beneath the free surface," Geophysical Journal International **166**, 1424–1439 (2006).

[77] C. Van der Veen, "Fracture mechanics approach to penetration of surface crevasses on glaciers," Cold Regions Science and Technology **27**, 31–47 (1998).

[78] J. Weertman, "Theory of water-filled crevasses in glaciers applied to vertical magma transport beneath oceanic ridges," Journal of Geophysical Research **76**, 1171–1183 (1971).

[79] D. G. Vaughan, "Tidal flexure at ice shelf margins," Journal of Geophysical Research: Solid Earth **100**, 6213–6224 (1995).

[80] M. J. Heap, M. Villeneuve, F. Albino, J. I. Farquharson, E. Brothelande, F. Amelung, J. L. Got, and P. Baud, "Towards more realistic values of elastic moduli for volcano modelling," Journal of Volcanology and Geothermal Research **390**, 106684 (2020).

[81] H. Mader, E. Llewellin, and S. Mueller, "The rheology of two-phase magmas: A review and analysis," Journal of Volcanology and geothermal Research **257**, 135–158 (2013).

[82] Y. Wada, "On the relationship between dike width and magma viscosity," Journal of Geophysical Research **99**, 743–755 (1994).

[83] D. Roman, A. Soldati, D. B. Dingwell, B. F. Houghton, and B. Shiro, "Earthquakes indicated magma viscosity during kīlauea's 2018 eruption," Nature **592**, 237–241 (2021).

[84]P. Traversa, V. Pinel, and J. Grasso, "A constant influx model for dike propagation: Implications for magma reservoir dynamics," Journal of Geophysical Research: Solid Earth **115** (2010).

[85]M. Balme, V. Rocchi, C. Jones, P. Sammonds, P. Meredith, and S. Boon, "Fracture toughness measurements on igneous rocks using a high-pressure, high-temperature rock fracture mechanics cell," Journal of Volcanology and Geothermal Research **132**, 159–172 (2004).

[86]M. P. Fischer, R. B. Alley, and T. Engelder, "Fracture toughness of ice and firn determined from the modified ring test," Journal of glaciology **41**, 383–394 (1995).

[87]M. Rist, P. Sammonds, S. Murrell, P. Meredith, C. Doake, H. Oerter, and K. Matsuki, "Experimental and theoretical fracture mechanics applied to antarctic ice fracture and surface crevassing," Journal of Geophysical Research: Solid Earth **104**, 2973–2987 (1999).

[88]G. Holdsworth, "Primary transverse crevasses," Journal of Glaciology **8**, 107–129 (1969).

[89]R. S. J. Sparks and H. E. Huppert, "Density changes during the fractional crystallization of basaltic magmas: fluid dynamic implications," Contributions to Mineralogy and Petrology **85**, 300–309 (1984).